# Negative extreme events in gross primary productivity and their drivers in China during the past three decades

Weizhe Chen[a,b], Dan Zhu[b], Chunju Huang[a,c,*], Philippe Ciais[b], Yitong Yao[d], Pierre Friedlingstein[e], Stephen Sitch[f], Vanessa Haverd[g], Atul K. Jain[h], Etsushi Kato[i], Markus Kautz[j], Sebastian Lienert[k,l], Danica Lombardozzi[m], Benjamin Poulter[n], Hanqin Tian[o], Nicolas Vuichard[b], Anthony P. Walker[p], Ning Zeng[q]

[a] State Key Laboratory of Biogeology and Environmental Geology, School of Earth Sciences, China University of Geosciences, Wuhan 430074, China
[b] Laboratoire des Sciences du Climat et de l'Environnement, CEA-CNRS-UVSQ, Gif-sur-Yvette 91191, France
[c] Laboratory of Critical Zone Evolution, School of Earth Sciences, China University of Geosciences, Wuhan 430074, China
[d] Sino-French Institute for Earth System Science, College of Urban and Environmental Sciences, Peking University, Beijing 100871, China
[e] College of Engineering, Mathematics, and Physical Sciences, University of Exeter, Exeter EX4 4QE, UK
[f] University of Exeter, Exeter EX4 4QE, UK
[g] CSIRO Oceans and Atmosphere, Canberra 2601, Australia
[h] Department of Atmospheric Sciences, University of Illinois, Urbana, IL 61801, USA
[i] Institute of Applied Energy (IAE), Minato, Tokyo 105-0003, Japan
[j] Forest Research Institute Baden-Württemberg, Freiburg 79100, Germany
[k] Climate and Environmental Physics, Physics Institute, University of Bern, Bern, Switzerland
[l] Oeschger Centre for Climate Change Research, University of Bern, Bern, Switzerland
[m] Climate and Global Dynamics Division, National Center for Atmospheric Research, Boulder, CO 80302, USA
[n] NASA Goddard Space Flight Center, Biospheric Science Laboratory, Greenbelt, MD 20771, USA
[o] International Center for Climate and Global Change Research, School of Forestry and Wildlife Sciences, Auburn University, 602 Duncan Drive, Auburn, AL 36849, USA.
[p] Environmental Sciences Division & Climate Change Science Institute, Oak Ridge National Laboratory, Oak Ridge, TN 37831, USA
[q] Department of Atmospheric and Oceanic Science, University of Maryland, College Park, MD 20742-2425, USA

* Corresponding author. E-mail address: huangcj@cug.edu.cn (C. Huang).

## Abstract

Climate extremes have remarkable impacts on ecosystems and are expected to increase with future global warming. However, only few studies have focused on the extreme ecological events and their drivers in China. We therefore carried out an analysis of negative extreme events in gross primary productivity (GPP) in China and the sub-regions during 1982-2015, using monthly GPP simulated by 12 process-based models (TRENDYv6) and an observation-based model (Yao-GPP). Extremes were defined as the negative 5th percentile of GPP anomalies, which were further merged into individual extreme events using a three-dimensional contiguous algorithm. Spatio-temporal patterns of negative GPP anomalies were analyzed by taking the 1000 largest extreme events into consideration. Results showed that the effects of extreme events decreased annual GPP by 2.8% (i.e. 208 TgC year$^{-1}$) in TRENDY models and 2.3% (i.e. 151 TgC year$^{-1}$) in Yao-GPP. Hotspots of extreme GPP deficits were mainly observed in North China (-53 gC m$^{-2}$ year$^{-1}$) in TRENDY models and Northeast China (-42 gC m$^{-2}$ year$^{-1}$) in Yao-GPP. For China as a whole, attribution analyses suggested that extreme low precipitation was associated with 40%-50% of extreme negative GPP events. Most events in northern and western China could be explained by meteorological droughts (i.e. low precipitation) while GPP extreme events in southern China was more associated with temperature extremes, such as cold spells in South China. The impacts of heat wave and drought are noticeable because GPP is much more sensitive to heat/drought than to cold/wet during extreme events. Combined with projected changes in climate extremes in China, GPP negative anomalies caused by drought events in northern China and by temperature extremes in southern China might be more prominent in the future.

Key words: Climate change; Extreme events; Gross primary production; Power law distribution; China

## 1. Introduction

Gross primary productivity (GPP) is the largest carbon flux, changes of which affect the whole terrestrial carbon cycle. The $CO_2$ fertilization and growing season extension are expected to enhance vegetation growth and increase terrestrial net primary productivity (Los, 2013; Piao et al., 2013; Zhu et al., 2016). However, at the same time, it has been suggested that climate extremes may alter the composition, structure and function of ecosystems and therefore have potential negative impacts on terrestrial carbon uptake (Du et al., 2018; von Buttlar et al., 2018). For instance, the 2003 extreme heat wave and drought in Europe caused up to 30% reduction in GPP and resulted in a strong anomalous net source of $CO_2$ (Ciais et al., 2005). Based on the commonly used definition of climate extremes, IPCC (2012) pointed out that changing climate has led to changes in the frequency, intensity, spatial extent, duration, and timing of weather and climate extremes, and can result in unprecedented impacts on terrestrial carbon cycle. Furthermore, climate change is projected to further increase the frequency, persistence and intensity of climate extremes in the mid- to late 21st century because of the on-going global warming (IPCC, 2013; Niu et al., 2017; Sui et al., 2018), which makes the impacts of future climate change on terrestrial ecosystem more uncertain (Samaniego et al., 2018; Yao et al., 2019). Therefore, characterizing extreme events is an important step for the development of adaptation strategies and risk reduction in the context of future climate change.

Extreme events are generally defined as statistically extreme or unusual episodes or occurrences, which are beyond the bounds of typical or normal variability (Reichstein et al., 2013). In scientific literature, extreme events have been defined in several ways—both from climatic and impact perspectives (Felton and Smith, 2017). Lloyd‐Hughes (2012) firstly proposed a novel 3-dimensional (longitude, latitude, time) structure-based approach to describe drought events. Zscheischler et al. (2013) further improved the method and performed the first global analysis of spatio-temporally contiguous carbon-cycle extremes. This method has advantages in analyzing the size, shape, temporal evolution and other interesting quantities of extreme events. By using this technique, Zscheischler et al. (2014a) demonstrated that the largest 1000 negative GPP extremes accounted for a decrease in global photosynthetic carbon uptake of approximately 3.5 PgC year$^{-1}$, with most events being attributable to water scarcity. Huang et al. (2016) quantified sensitivities of GPP to spatio-temporally contiguous hydrological extreme events and implied that vegetation in Earth System Models (ESMs) was on average more sensitive to droughts than observed. Zscheischler et al. (2018) pointed out that traditional assessment methods which considered only one driver at a time underestimated risk from extreme events, highlighting a better understanding of compound events. Model output of the Coupled Model Intercomparison Project Phase 5 (CMIP5) future projections suggested that negative extremes in GPP would be driven by concurrent dry and hot conditions during the 21st century (Zscheischler et al., 2014d).

The negative impacts of climate extremes on natural ecosystems and agriculture have been widely reported in China. Yuan et al. (2016) found that the 100-year return heat wave and drought in the summer of 2013 in southern China significantly reduced regional GPP, and produced the largest negative crop yield anomaly since 1960. The anomalous 2008 ice storm episode resulted in increased vegetation mortality, which exceeded recruitment for evergreen and deciduous broad-leaved species in central China (Ge et al., 2015). The most severe spring drought over the last five decades in 2010 in southwestern China reduced regional annual GPP by 4%, producing the lowest annual GPP over the period 2000–2010 (Zhang et al., 2012). Dynamic Land Ecosystem Model-based analysis showed that drought stress led to a large reduction of crop yield in China (Ren et al., 2012), with the maximum reduction in crop yield (−17.5%) occurred in 2000, a year with extreme drought and relatively high $O_3$ concentrations (Tian et al., 2016). The temperature and precipitation anomalies were the principal drivers of Normalized Difference Vegetation Index (NDVI) variation in the Yangtze River Basin (YRB) in recent years (Cui et al., 2018). These regional studies or case studies improved our understanding of the vulnerability and response of terrestrial ecosystems to individual extreme climate events. Nevertheless, most previous studies in China mainly focus on either the impacts of climate extremes (Chen et al., 2018; Yao et al., 2017; Yuan et al., 2016) or only a few cases of extreme ecological events (Yuan et al., 2016; Zhang et al., 2012) but did not analyze a large number of extreme events in GPP in a systematic approach.

The sensitivity and vulnerability of ecosystem productivity to climate variability are expected to vary widely in different ecosystems and different climate zones, affected also by biodiversity or management practices (Isbell et al., 2015; Wang et al., 2017; Yao et al., 2018).

China has different climate zones that range from tropic in the south to subarctic zone in the north, comprising wide ranges of precipitation and temperature gradients. However, there are a limited number of studies on the effects of multiple climate drivers on GPP in China. Thus, we intend to provide a statistical analysis of extreme events in GPP and their drivers at the national scale and the nine sub-regions (Fig. 1a). This study aims to (1) diagnose the spatial and temporal patterns of extreme events in GPP in China; (2) attribute these extreme events to climatic drivers; (3) explore size distribution of extreme ecological events for different climate drivers and different regions. We expect to provide a better understanding of the characteristics of extreme events and their responses to different drivers.

## 2. Materials and methods

### 2.1. GPP data sources

**Table 1**

Summary of monthly GPP estimates, climate and fire data used in this study. Some of the datasets extend beyond 1982–2015, but the analysis in this paper is confined to those years.

| Dataset | Variable | Resolution | Period | Citation |
| --- | --- | --- | --- | --- |
| Yao-GPP | GPP | 0.1° | 1982-2015 | (Yao et al., 2018) |
| Historical climate carbon cycle model intercomparison project (TRENDYv6) | GPP and soil moisture | 0.5°-1° | 1982-2015 | (Le Quéré et al., 2018) |
| Institute of Tibetan Plateau Research, Chinese Academy of Sciences (ITPCAS) | Air temperature and precipitation | 0.1° | 1982-2015 | (Chen et al., 2011) |
| Climatic Research Unit (CRU) | Air temperature and precipitation | 0.5° | 1982-2015 | (Harris et al., 2014) |
| Climatic Research Unit (CRU) | self-calibrating Palmer Drought Severity Index | 0.5° | 1982-2015 | (van der Schrier et al., 2013) |
| Global Fire Emissions Database, Version 4 (GFEDv4) | Burned area and fire emissions | 0.25° | 1997-2015 | (Randerson et al., 2017) |

Results from an observation-based model of GPP (Yao-GPP, hereafter and Table 1), with 0.1° spatial resolution and monthly temporal frequency over China, were obtained from Yao et al. (2018). This GPP data is developed using a machine learning technique, model tree ensembles (MTE) (Jung et al., 2011) with eddy flux measurements from 40 sites in China and the surrounding countries. The high-resolution GPP data can successfully capture the spatio-temporal variations of the GPP observed at the flux sites, including validation flux sites that were not part of the MTE training set (Yao et al., 2018).

Besides the above observation-based model, we also used monthly GPP from process-based ecosystem models that took part in the historical climate carbon cycle model intercomparison project (TRENDYv6, Table A.1). The model simulations all followed the same experimental protocol (Le Quéré et al., 2018; Sitch et al., 2015) and were driven with the same climate data from the Climatic Research Unit and National Center for Environmental Prediction (CRU-NCEP) climate forcing reconstruction. The GPP outputs were from the S3 TRENDY simulations which used observed $CO_2$ concentrations, changing climate, and land cover changes as forcing over the period 1860–2016. Many different process-based models were used in TRENDY simulations. As coarse spatial resolution makes it not possible to diagnose enough GPP extreme events, model simulations with coarser resolution than 1° were excluded. Consequently, 12 models were finally selected: CABLE (Haverd et al., 2017), CLM4.5 (Oleson et al., 2013), DLEM (Tian et al., 2015), ISAM (Jain et al., 2013), LPJ-GUESS (Smith et al., 2014), LPJ-wsl (Sitch et al., 2003), LPX-Bern (Keller et al., 2017), ORCHIDEE (Krinner et al., 2005), ORCHIDEE-MICT (Guimberteau et al., 2018), SDGVM (Woodward et al., 1995), VEGAS (Zeng et al., 2005) and VISIT (Kato et al., 2013), and see references and further model details contained in Le Quéré et al. (2018).

## 2.2. Climatic data

To attribute negative extreme events in GPP to drivers, we used air temperature (Ta), precipitation (P), soil moisture (SM), self-calibrating Palmer Drought Severity Index (scPDSI) (van der Schrier et al., 2013), burned area (BA) and $CO_2$ emissions from fires (FE) (Table 1). Gridded Ta and P data (0.5° spatial resolution) was taken from the monthly dataset compiled by the CRU of the University of East Anglia, UK. This CRU datasets span the period 1901-2015 and can be obtained at http://www.cru.uea.ac.uk/data. As Yao-GPP was driven by another forcing dataset, which was developed by Data Assimilation and Modeling Center for Tibetan Multi-spheres, Institute of Tibetan Plateau Research, Chinese Academy of Sciences (ITPCAS, http://westdc.westgis.ac.cn), the corresponding monthly Ta and P (Fig. A.1) were used to identify the driving factors for Yao-GPP. We used the respective SM data from TRENDY models to diagnose the contribution of SM to their GPP extremes. As for Yao-GPP, averaged TRENDY SM was used in attribution analysis. The scPDSI data, which represents an index for comparing the relative spatio-temporal variability of soil moisture changes over wide regions, was also collected from CRU. The Global Fire Emissions Database, Version 4 (GFEDv4) provides global estimates of monthly burned area and carbon emissions from fire (https://daac.ornl.gov/VEGETATION/guides/fire_emissions_v4.html). This data has a 0.25° spatial resolution and is available from July 1997 through 2015.

## 2.3. Preprocessing method

All of the gridded datasets were first resampled to 0.1° × 0.1° spatial resolution using the nearest neighbor interpolation. The original GPP and climate variables contain long-term trends and strong seasonal cycles. For these variables (i.e. Ta, P, scPDSI, SM and all the GPP data), the temporal linear trend and mean seasonal cycle were removed in each grid cell to get the anomalies of the time series data. For the variables describing episodic events (BA and FE), we divided them by the total sum of the respective time series in each grid cell. The preprocessing produced anomalies in de-trended GPP and climate, which represents deviations from the mean behavior (Zscheischler et al., 2013).

## 2.4. Negative extreme events detection

In scientific literature, extremes are usually defined based on either the probability of occurrence of given quantities or threshold exceedances (IPCC, 2012). In order to quantify the extreme ecological events, we defined extremes as the negative 5th percentile of all the GPP anomalies (derived from the above-mentioned preprocessing). Contiguous extreme negative GPP anomalies (i.e. voxels) are further merged into individual extreme events following Zscheischler et al. (2014a). By "contiguous", we mean any of the 26 neighbors in three-dimensional (latitude × longitude × time) space also experiencing an extreme GPP anomaly. The size of an extreme event is the summation of GPP anomalies over the spatio-temporal domain of the event cluster. With this algorithm, each GPP datasets produced 1000~5000 extreme events for the whole China during the study period. As we are more interested in large events and hope to compare between models, we investigated the 1000 largest negative extreme events in GPP ($GPP_{1000}$) for the whole China and the 100 largest extreme events for each of the nine sub-regions.

## 2.5 Power laws identification

Power laws in frequency or size distributions were previously detected in a variety of natural phenomena (Clauset et al., 2009), such as global fire size distributions (Hantson et al., 2015) as well as intensities of earthquakes. In this study, we want to analyze the size distribution of extreme ecological events for different climate drivers and different regions in China. According to Zscheischler et al. (2013), the size distribution of extreme events ($s_e$) can also be well approximated by a power law relationship as follows:

$$p(s_e) \sim s_e^{-\alpha} \qquad (1)$$

where $\alpha$ is a constant parameter of the distribution known as the exponent or scaling parameter. The exponent $\alpha$ of the size distribution was diagnosed using the fitting technique of maximum likelihood presented by Clauset et al. (2009). This algorithm has been widely applied in diagnosing power law distributions in empirical data (Scannell et al., 2016). The $\alpha$-value from the power-law function provides information on asymmetry in the size distribution of extreme events, indicating the relative number of extreme events of different sizes. An increase in $\alpha$ suggests an increasing proportion of small extreme events relative to large ones. It can also be used as an index to investigate the different patterns in extreme events for different drivers and regions. Clauset's method provides a goodness-of-fit parameter p-value, where p-value > 0.1 indicates a good fit.

## 2.6. Attribution of negative extreme events

In order to identify possible drivers of individual negative extreme events in GPP, we adopted the attribution method from Zscheischler et al. (2013). For each event, we calculate the median of driver variable anomalies over the spatio-temporal domain of the event, which directly represents the anomaly intensity of the corresponding driver during the event. Then, we let the event shift in each time step and obtain a series of medians ($M_s$) as a function of time. As there are possibly lagged responses of ecosystems to all these drivers (Reichstein et al., 2013), we consider time lags of a maximum of three months. Then, if any of the medians within three months preceding the events is less (higher) than the 10th (90th) percentile of $M_s$, the driver (e.g. a cold spell or heat wave) is selected as influential for that event. An GPP extreme event is attributed to fire if either BA or $CO_2$ emissions from fires during the event is higher than 90th percentile. A single event is possible to be explained by multiple drivers. The attribution rate is defined as the proportion of studied events, which are attributed to any of the nine drivers (i.e. for all drivers) or a typical driver (e.g. for cold spell).

## 2.7 GPP sensitivity during the extreme events

We explored GPP sensitivity of different models to precipitation or temperature anomalies (i.e. heat wave, cold spell, drought and wet). For each model, the single driver induced extreme GPP events were selected in order to extract the impact of this driver from potential additive effect. And then, we divided the mean GPP anomalies by mean precipitation or temperature anomalies over the voxels in selected extreme events. For example, the GPP sensitivity to drought is expressed as:

$$Sens_{-p} = \frac{|\overline{GPP}_{an,-P}|}{|\bar{P}_{an,-P}|} \qquad (2)$$

where $\overline{GPP}_{an,-P}$ is averaged GPP anomalies over all voxels from exclusively drought (i.e. low P) induced extreme events among the studied 1000 events; $\bar{P}_{an,-P}$ is averaged precipitation anomalies over the same voxels. Thus, $Sens_{-p}$ is the sensitivity of modelled GPP to the driver, that is GPP deficit for each precipitation anomaly during extreme events.

# 3. Results

## 3.1. Spatio-temporal patterns of extreme events

Most (95%) of the $GPP_{1000}$ had a duration of 1-7 months (Fig. A.2). To map spatial distribution of GPP anomalies, the $GPP_{1000}$ over China were aggregated in time. In details, for a specific location, all anomalies in GPP classed as extreme events were summed and then divided by 34 years. TRENDY multi-model median showed hotspots of extreme events in North China where the GPP extreme anomalies could reach up to -70 gC m$^{-2}$ year$^{-1}$ (Fig. 1a). In addition, regional medians of North China, Inner Mongolia and Central China had prominent GPP extreme anomalies of -53, -31 and -30 gC m$^{-2}$ year$^{-1}$, respectively. In contrast, both Northwest China and Qinghai-Tibetan Plateau (QTP) were less impacted by extreme events with regional median GPP anomalies of approximately -10 gC m$^{-2}$ year$^{-1}$.

According to the Yao-GPP data-driven model, the anomalies became larger in magnitude from southeast to northwest (Fig. 1b). The lowest impacts were diagnosed with GPP deficits of less than -10 gC $m^{-2}$ $year^{-1}$ in Southwest China and Sichuan Basin where there are relatively lower altitudes. The largest negative GPP extreme events were diagnosed in Inner Mongolia (-46 gC $m^{-2}$ $year^{-1}$), Northeast China (-42 gC $m^{-2}$ $year^{-1}$) and North China (-28 gC $m^{-2}$ $year^{-1}$) in Yao-GPP. The prominent extreme events were generally diagnosed in mountainous regions such as Qinling Mountains in North China around Sichuan Basin, and Greater Khingan Mountains and Changbai Mountains in Northeast China. Although these regions had less GPP than South China, much more significant GPP deficits were detected. Hot spots of extreme events were detected in Northeast China for Yao-GPP but in North China for the process-based ecosystem models. Compared with Yao-GPP, the process-based ecosystem models overestimate the magnitude of extreme events in Northeast China and underestimate in North China (Fig. 1d). Disagreement between the process-based ecosystem models was mainly found in North China and South China (Fig. 1c).

The $GPP_{1000}$ were aggregated in space to produce the monthly evolution of GPP anomalies in China, which was further aggregated to show seasonal differences (Fig. 2). The median over the TRENDY models indicated that extreme events in summer produced the most GPP negative anomalies by -30.4 TgC $mon^{-1}$, which accounted for 45% anomalies of the year, followed by spring, autumn and winter. Boxplot exhibited that LPX-Bern was an outlier in summer and autumn while VISIT was an outlier in winter over the 12 process-based models because of their overestimates of GPP deficits. The GPP deficits in Yao-GPP were smaller than the TRENDY median in spring, autumn and winter but slightly larger in summer, which consequently made the summer accounting for 68% of the mean annual anomalies in Yao-GPP. Among the 12 TRENDY models, LPX-Bern produced the largest extreme events by -475.2 TgC $year^{-1}$ while DLEM produced the smallest extreme events by -98.4 TgC $year^{-1}$ for the $GPP_{1000}$ in China (Fig. A.3). The TRENDY median and Yao-GPP estimated values of -207.6 TgC $year^{-1}$ and -151.2 TgC $year^{-1}$ for the sum of the $GPP_{1000}$, accounting for 2.8% and 2.3% of mean annual GPP, respectively.

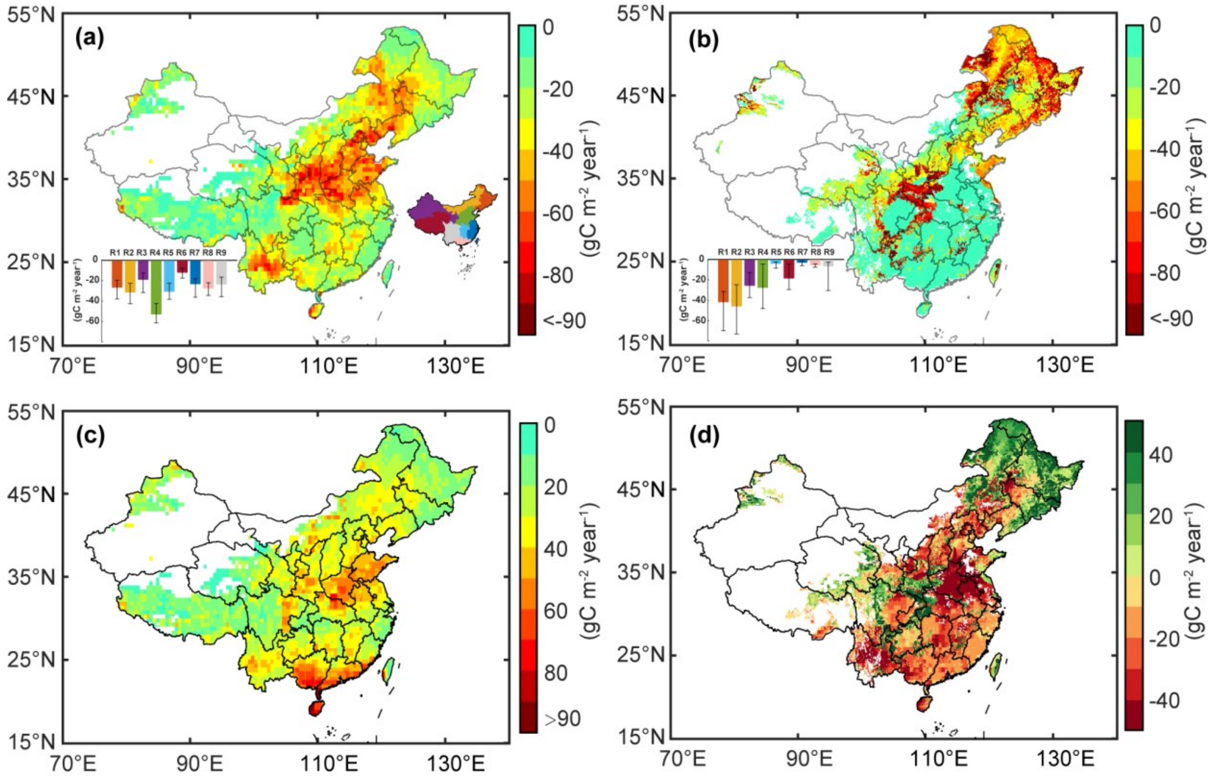


**Fig. 1.** Spatial distributions of (a) the magnitude of the 1000 largest negative extreme events in GPP ($GPP_{1000}$) during 1982-2015 from the median of the 12 process-based TRENDY models and (b) the observation-based GPP model Yao-GPP, (c) standard deviation over TRENDY models and (d) the TRENDY median minus Yao-GPP (i.e. panel (a) minus panel (b)). The left insets in panel (a) and (b) denote the median (i.e. bar graph), 25th and 75th percentile (i.e. error bar) of GPP anomalies for each sub-region. The right inset in panel (a) presents the definition of the nine sub-regions in China. R1 (red): Northeast China; R2 (orange): Inner Mongolia; R3 (purple): Northwest China; R4 (green): North China; R5 (sky blue): Central China; R6 (dark red): Qinghai-Tibetan Plateau (QTP); R7 (dark blue): Southeast China; R8 (pink): South China, and R9 (grey): Southwest China.

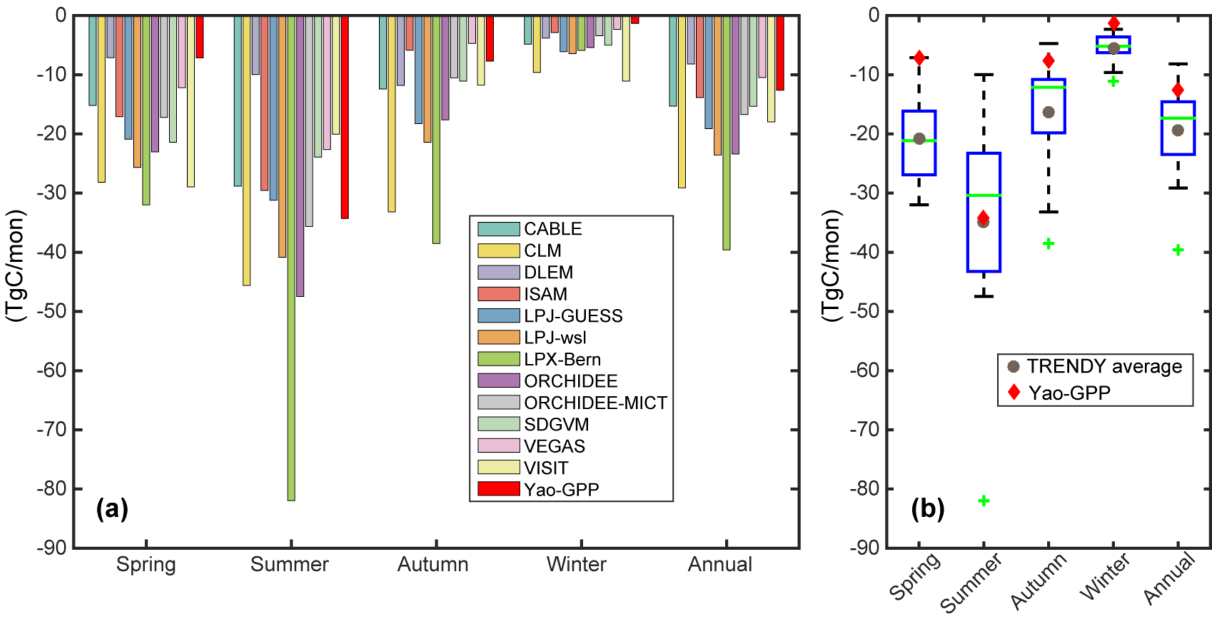


**Fig. 2.** (a) Bar graph and (b) boxplot of GPP extremes in four seasons and annual mean. The legend in panel (a) distinguishes the 13 GPP datasets. The red diamonds and gray dots in panel (b) represent Yao-GPP and averages over the 12 process-based models, respectively. The lower and upper edges of the box indicate 25th and 75th percentile of the GPP anomalies over the 12 process-based models. The green line and cross are median and outliers, respectively. Note that 1 TgC = $10^{12}$ gC.

3.2. Attribution of negative GPP extremes in China and the nine sub-regions

The eight climate indices and fire variables were regarded as potential drivers of the $GPP_{1000}$ in China. As for single climate drivers, we investigated both positive and negative anomalies in Ta, P, SM and scPDSI (Fig. 3a). According to the multi-model median, both cold spell and heat wave were influential for ~26% of the extreme events. Meteorological droughts (i.e. low P) were associated with ~58% of the extreme events, making it the major driver among the nine indices. In addition, extreme events were more related to droughts than floods as low P, low scPDSI and low SM accounted for much more events than the corresponding positive values of those indices (i.e. high P, high scPDSI and high SM). But in the arguably more realistic Yao-GPP dataset, cold spell explained 36% of the extreme events, which was much larger than heat wave (18%). Drought indices were associated less extreme negative events than wet indices, which was different from the TRENDY model results. The 10% significance threshold denotes that $GPP_{1000}$ in Yao-GPP were nearly independent of SM, scPDSI and fire indices. As GPP extreme events are mainly driven by Ta and P anomalies in China at national scale, we explored the possible compound T&P effects (Fig. 3b). The $GPP_{1000}$ from TRENDY models and Yao-GPP were significantly associated with P anomalies (both wet and drought) during normal Ta condition. No significant compound T&P effects were observed for TRENDY models and only significant compound cold and wet conditions were linked to GPP extreme events in Yao-GPP.

China has different climate zones so that the response of GPP extreme events to driver indices are expected to be different across those zones. As shown in Fig. 4, the TRENDY median indicated that extreme events in most sub-regions were mostly associated with low P, especially for North China (66%) and Inner Mongolia (62%), but not in South China (37%). In contrast, temperature extremes (i.e. cold spell or heat wave) explained more extreme events in southern China (60%-70%) than in northern China (30%-50%). For comparison with the different response to low P, the impacts of soil drought (i.e. low SM and low scPDSI) were rather stable and explained 35%-40% and 25%-30% among all sub-regions in China. In particular, low SM was associated with 42% of extreme events, followed by low P (38%) and cold spell (34%) in Southeast China. This suggested a decoupling between P and SM in controlling GPP extremes, with P anomalies combined with Ta anomalies enhancing evapotranspiration and decreasing SM in southern China to cause GPP extremes being more influenced by SM than by just P. The Yao-GPP also presented the different vulnerability of extreme events in GPP to temperature extremes between northern and southern China. Compared with Yao-GPP, the TRENDY models largely underestimated attribution rate for high P in most sub-regions but overestimated attribution rate for low P in northern China. For the period of 1997-2015, both Yao-GPP and TRENDY median indicated that fire was linked to 20% of large events in South China and Southeast China. In terms of compound T&P effects (Fig. A.5), we found the $GPP_{100}$ from TRENDY were significantly associated with concurrent heat and drought events in Northwest China, Inner Mongolia, North China, Central China and Southeast China. But in Yao-GPP, $GPP_{100}$ in most sub-regions of China were linked to compound cold and wet events.

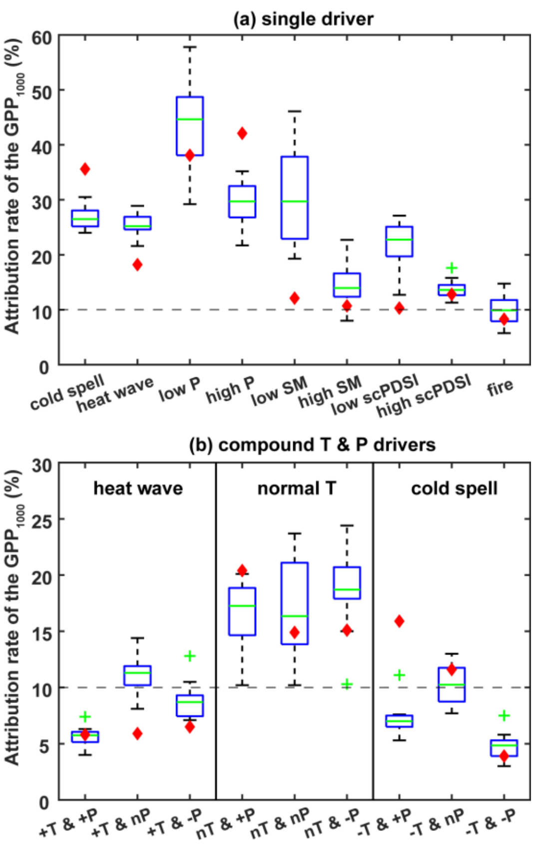

**Fig. 3.** Attribution rate of the $GPP_{1000}$ for single or compound drivers. Boxplots result from the TRENDY models and red diamonds are for Yao-GPP. The horizontal dashed lines denote the significance threshold (10%), below which the driver and GPP variation are expected to be independent. The nT and nP in panel (b) represent normal Ta (i.e. not extreme Ta condition) and normal P, respectively. The attribution of the $GPP_{1000}$ in China for each model is shown in Fig. A.4.

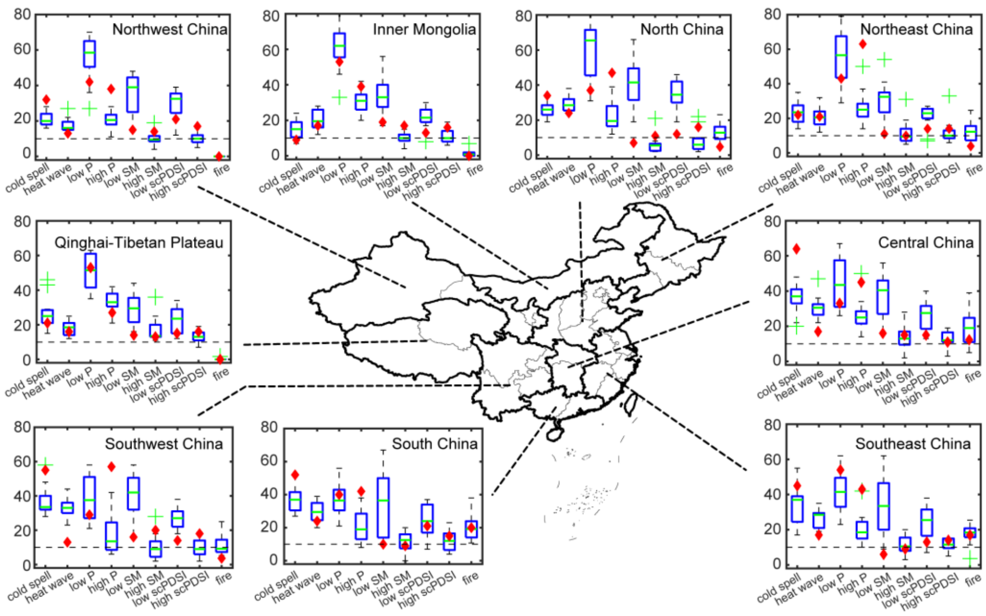


**Fig. 4.** Attributions rate (%) of GPP extreme events to climate drivers and fire in the nine sub-regions of China. The largest 100 negative extreme events ($GPP_{100}$) were used for each sub-region.

3.3. Size distribution of GPP extreme events

In order to understand the characteristic of extreme events, it is crucial to know the size distribution of extreme events. The sizes of the $GPP_{1000}$ from the 13 GPP datasets were well fitted by power law distributions (Fig. 5). The power law exponent ($\alpha$-value) agreed well among the 13 datasets, ranging from 1.57 to 1.76, with the highest value in Yao-GPP and the lowest value in ORCHIDEE-MICT. The median $\alpha$-value ($\alpha_m$-value) over the TRENDY models was 1.68, which is slightly smaller than $\alpha$-value in Yao-GPP ($\alpha_Y$-value = 1.76).

It was found that different climate regions and vegetation types resulted in different $\alpha$-value of fire size distribution (Hantson et al., 2015). Therefore, we supposed that size distribution of extreme events could have variations for different drivers and in sub-regions. As for the TRENDY models, the $\alpha_m$ had substantial fluctuation between 1.52-2.18 for different drivers (Fig. 6). The smallest $\alpha_m$-value was observed for low SM (1.53, the range of 1.47-1.76 in TRENDY models) and low scPDSI (1.52, the range of 1.40-1.68 in TRENDY models) related extreme events and the largest $\alpha_m$-value (2.18, the range of 2.06-3.05 in TRENDY models) was diagnosed for fire related extreme events (Table A.2). It means that low SM tended to result in large GPP negative anomalies respective to small events while fire was more associated to small sized extreme events in China. Furthermore, all $\alpha_m$-values for drought induced extreme events, including meteorological drought (i.e. low P) and soil drought (i.e. low SM and low scPDSI), were significantly smaller than wet related events. Similarly, the Yao-GPP also showed that low SM (2.09) and low scPDSI (2.18) were correspondingly smaller than high SM (2.18) and high scPDSI (2.22) related events, suggesting more vulnerability of GPP to drought events than extreme wet events. Compared with $\alpha_Y$-values, $\alpha_m$-values were overall underestimated. Similarly, the $\alpha$-values for the $GPP_{100}$ for each sub-region in China were also diagnosed (Fig. A.6). Clear spatial decreasing gradients in $\alpha_m$-values were found from the northwest to the southeast, indicating relatively more large-events were diagnosed in Southeast China (1.65) and North China (1.65).

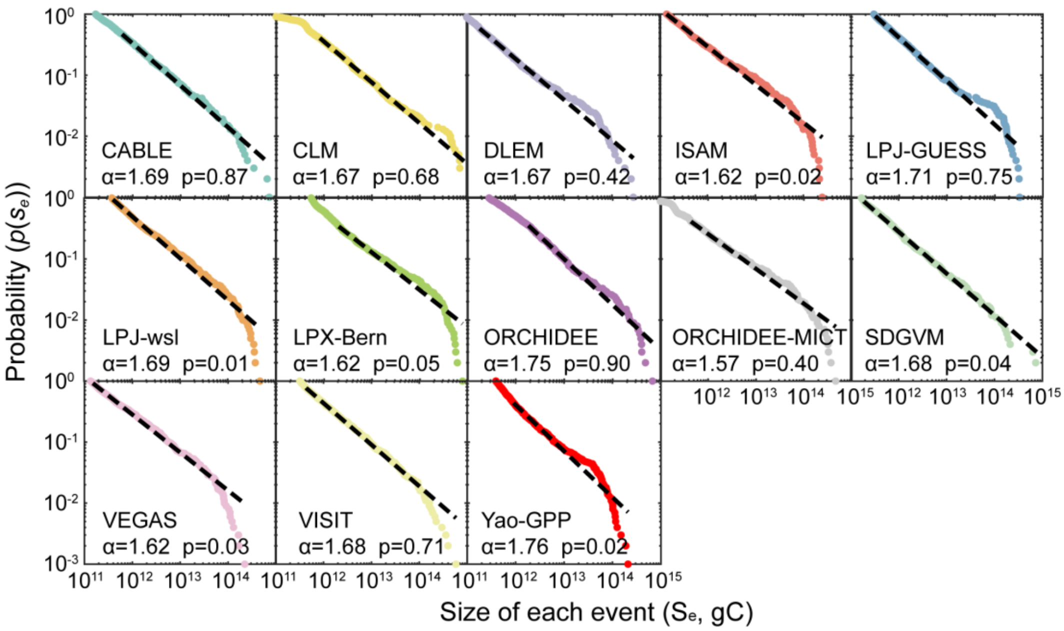


**Fig. 5.** Fitted power law distributions to sizes of negative GPP anomalies (gC) for the 13 GPP datasets. The letter $\alpha$ denotes the exponent of the fitted power law. Colored dots are the $GPP_{1000}$ for each dataset and black dashed lines are fitted power law distribution. A p-value > 0.1 indicates a good fit.

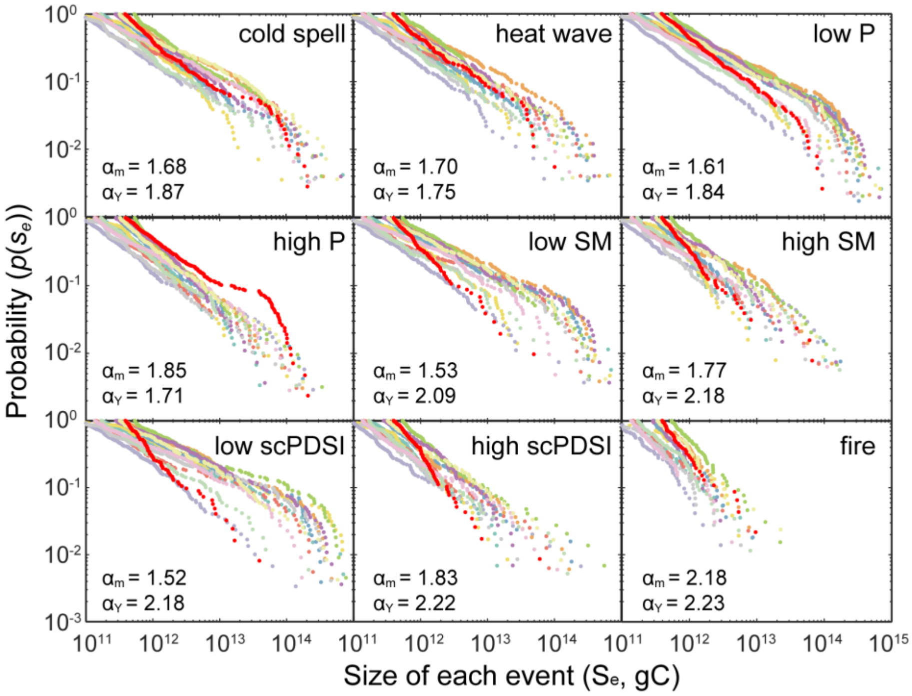


**Fig. 6.** Probability distributions of sizes of extreme events caused by the nine drivers, respectively. The color legend to distinguish GPP datasets is the same as Fig. 2. The letter $\alpha_m$ and $\alpha_Y$ are median of the fitted exponents over the TRENDY models and exponent for Yao-GPP, respectively. The sample size, power law fitting and goodness-of-fit parameters are presented in Table A.2.

### 3.4 GPP sensitivity to temperature and precipitation anomalies

The impacts (anomalies) of the extreme events is also determined by models' sensitivity. Thus, we explored the GPP sensitivities of the models to evaluate the model performance during extreme events (Fig. 7). The GPP sensitivities of Yao-GPP to heat, cold, wet and drought were 118 gC $m^{-2}$ $month^{-1}$ °$C^{-1}$, 29 gC $m^{-2}$ $month^{-1}$ °$C^{-1}$, 1.8 gC $m^{-2}$ $mm^{-1}$ and 4.1 gC $m^{-2}$ $mm^{-1}$, respectively. Compared with Yao-GPP, the TRENDY median underestimated the sensitivities to heat (-18%) and drought (-42%) but overestimated the sensitivities to cold (37%) and wet (16%). Nevertheless, both TRENDY median and Yao-GPP demonstrated significantly higher GPP sensitivities to heat and drought than to cold and wet (i.e. heat/cold > 1, drought/wet > 1), highlighting the negative impacts of heat and drought events.

The GPP sensitivity to temperature or precipitation anomalies (i.e. heat, cold, wet and drought) vary significantly across the 13 models. For example, ORCHIDEE-MICT showed the same GPP sensitivities to heat, cold as well as heat/cold ratio as Yao-GPP, but presented less response to precipitation extremes. In fact, all the process-based models except DLEM showed less sensitive to drought than Yao-GPP. 12 out of the 13 models was more sensitive to heat than to cold events and 10 out of the 13 models was more sensitive to drought than to wet events. TRENDY models had remarkable disagreement in heat/cold sensitivity ratio but showed better agreement in drought/wet sensitivity ratio.

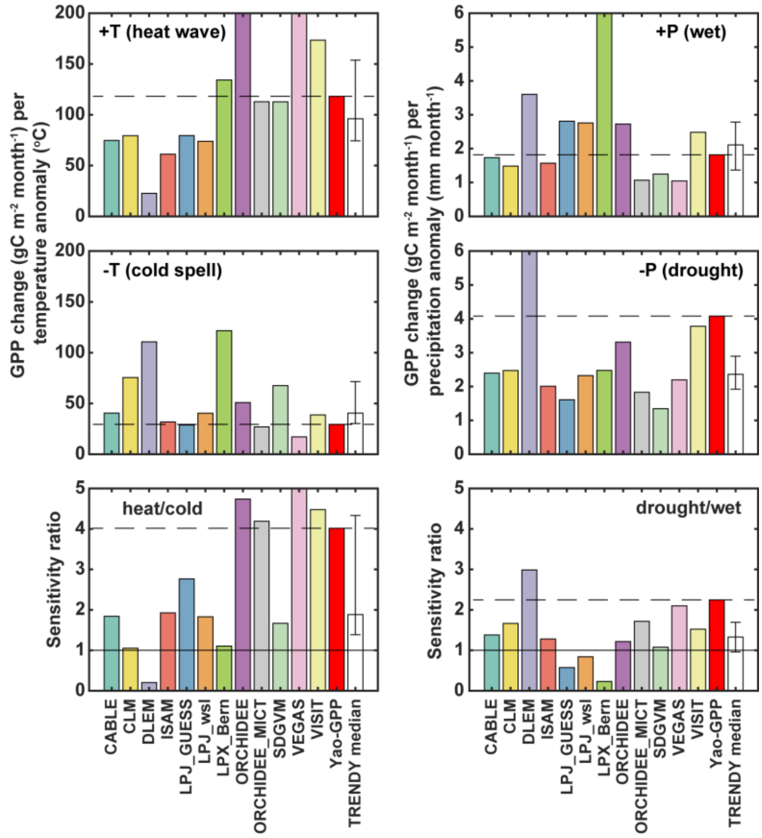


**Fig. 7.** Sensitivities of GPP anomalies to single driver of heat wave, cold spell, wet and drought during extreme events among the 13 models. The white bar in each panel shows TRENDT median, 25th and 75th percentile. The horizontal dashed line denotes Yao-GPP value.

## 4. Discussion

The characterization of extreme events in vegetation productivity is critical for understanding its role in regulating regional carbon cycles and its climatic drivers. As far as we know, this might be the first attempt to analyze spatio-temporally contiguous extreme GPP events at the national scale and sub-regions in China. Spatial distribution of negative extreme events from Yao-GPP exhibited hotspots in Northeast China and Qinling Mountains where high interannual variability was also diagnosed in Yao et al. (2018). Xu et al. (2012) also found that the area experiencing negative vegetation growth anomalies increased in northern China but decreased in southern China during 2000s, although the whole China experienced an increasing trend in heat waves and drought events. A strong negative NPP trend was diagnosed in Northeast China (Sitch et al., 2015), further emphasizing more concerns should be given to northern China. Based on four global GPP datasets, Zscheischler et al. (2014a) demonstrated that a few extreme events dominated global interannual variability in GPP. It could explain the similar spatial distribution between GPP negative extremes and interannual variability of GPP in most regions in China. This result highlights the importance of extreme events in regulating regional carbon cycles. In general, the effects of extreme events decreased annual GPP by 2.8% and 2.3% in TRENDY model and Yao-GPP, respectively. TRENDY median and Yao-GPP showed that extreme events in summer contributed to 45% and 68% of GPP negative anomalies, respectively, followed by spring, autumn and winter. This may be because summer usually corresponds to the highest GPP, and thus the highest absolute GPP anomalies are likely to occur when extreme events happen in summertime. For instance, in the summer of 2013, the strongest drought and heat wave on record for the past 113 years resulted in a 39–53% reduction of the annual net carbon sink of China's terrestrial ecosystems (Yuan et al., 2016).

The attribution analyses implied that low P explained 58% and 38% of the $GPP_{1000}$ in TRENDY models and Yao-GPP, respectively. In global drought-affected areas, the reduced carbon uptake could explain larger than 70% of the interannual variation in GPP (Du et al., 2018), also emphasizing the overall significantly negative impacts of meteorological droughts on vegetation productivity. Nevertheless, the vulnerability of GPP to these nine drivers showed marked difference between northern and southern China. A few mechanisms may explain the phenomenon that droughts were associated with much more extreme events in northern China (~60%) than in southern China (~40%) in TRENDY models. Firstly, the different climate is partly responsible for this different response that northern China experiences annual precipitation with less than 800 mm year$^{-1}$ while southern China is moister (Fig. A.1). In addition, consecutive dry days averaged over 1961–2015 for northern China is larger than 50 days year$^{-1}$, which is much higher than southern China (Shi et al., 2018). Secondly, southern China has much higher tree density (Crowther et al., 2015), while most regions of northern China (e.g. Inner Mongolia and Northwest China) are mainly dominated by grasslands (Yao et al., 2018). Grasslands are more susceptible to droughts in contrast to forests (Reichstein et al., 2013), probably because of shallower root system in grasslands (Teuling et al., 2010). However, compared with Yao-GPP, TRENDY models seem to overestimate the attribution rate to droughts (i.e. low P, low SM and low scPDSI) but underestimate the sensitivity to low P. The over-response of GPP and leaf area index in Earth system models to droughts has previously been suggested by Huang et al. (2016). Both types of GPP datasets demonstrated that vegetation in South China is mostly vulnerable to temperature extremes, in particular cold spells. This result is consistent with results from Xu et al. (2016) and Yao et al. (2018) that the sensitivity to temperature variability is higher in southern China, especially for forests. Compared with Yao-GPP, TRENDY models systematically underestimated cold spell-induced events and overestimated heat wave-induced events in southern China. A better representation of photosynthetic temperature acclimation in process-based models is critical to reduce the uncertainty in modeling the carbon cycle-climate feedback (Lombardozzi et al., 2015). Zscheischler et al. (2014d) highlighted the strong compound hot and dry events during 21st century based on CMIP5 future projections. We also found the significant impacts of concurrent hot and dry events in most sub-regions of China but the $GPP_{1000}$ were mostly associated with P anomalies during normal Ta for China as a whole.

The power law exponent of size distributions of extreme events in China is 1.68 in TRENDY median and 1.76 in Yao-GPP, which are consistent with that in Asia (1.61) and different continental range (1.55–1.75) as extracted by Zscheischler et al. (2014c). However, the exponent varied significantly for different drivers with the range of 1.49-2.09 for TRENDY models and 1.69-2.39 in Yao-GPP (Fig. 6). In addition, the power law exponent for drought-induced extreme events were significantly smaller than for wet-related events. It means drought events are more likely to result in relative large events while wet events provoke less GPP response. It was also supported by the plot between number of studied largest extreme events and attribution rate for P, SM and scPDSI indices (Figs. 8 and A.7). When we increased the number of studied events (i.e. when looking into the smaller events), the attribution rate shows significant decreases for all drought indices but increase for all wet indices. A case study in Inner Mongolia grassland ecosystems demonstrated that both aboveground net primary productivity and $CO_2$ fluxes in the semiarid steppe were very stable in the face of extreme large precipitation events, regardless of the timing of the events (Hao et al., 2017). In contrast, multiyear precipitation reduction over northern China significantly decreased water availability, indicated by the Palmer Drought Severity Index and soil moisture measurements, and further resulted in strong decreases in carbon uptake (Yuan et al., 2014). Therefore, the lower sensitivity of vegetation to wet events than to droughts in our results (Fig. 7) could explain the more decisive role of droughts for negative GPP events. Based on multiple terrestrial models, Zscheischler et al. (2014b) also suggested higher drought impacts on GPP anomalies, partially during compound hot and dry conditions. The $\alpha_m$-value for fire-induced extreme events is much lower than for climate drivers, implying that GPP in China is less vulnerable to fire than to climate extremes.

The on-going global warming increased extreme climate events are an increasing threat to vegetation productivity in the future (Frank et al., 2015). It has been suggested that warm extremes are more frequent and more persistent in a +2 ºC global warming scenario based on 29 climate models, especially in southern China (Sui et al., 2018). Accordingly, we could predict that southern China has to face more heat wave-induced GPP negative anomalies as it is highly vulnerable to warm extremes. The effect of cold spells in southern China is more noticeable but received less attentions than droughts. Liu et al. (2018) found that the extension of the growing season in the Northern Hemisphere may actually make plant in fact more vulnerable to frost days, which further highlights the important role of cold spell. In addition, increases in the total amount and frequency of wet extremes are projected over most regions of China, particularly in QTP (Niu et al., 2017; Sui et al., 2018), which we expect have less negative impacts on vegetation productivity of grasslands there. An experimental study showed that grassland plant diversity increases the resistance of ecosystem productivity to climate extremes (Isbell et al., 2015), which provides a potential strategy to face future climate extremes for a large area of grasslands in northern China. Both TRENDY models and Yao-GPP showed that less GPP deficits were observed in Sichuan basin (Fig. 1), where croplands are the dominant vegetation type, possibly implying the importance of management for mitigating damage from climate extremes. Nevertheless, we still could not rule out the damage of climate extremes on croplands as evidence also showed that droughts and heat wave episodes significantly reduced global and national crop production with a reduction in both harvested area and yields (Lesk et al., 2016; Piao et al., 2010). For instance, Lobell et al. (2012) argued that warming presented an even greater challenge to wheat than implied by previous modeling studies.

However, there are still some limitations in this study. Firstly, we only consider time lags of a maximum of three months. There is evidence that extreme events can affect the carbon cycle concurrently and produce lagged impacts at longer time scales (e.g. through vegetation mortality) (Arnone et al., 2008; Schwalm et al., 2017). This prolonged response of vegetation GPP could be discovered in case studies but is rather difficult to be detected by our approach. Secondly, there are ~10% of the $GPP_{1000}$ that did not correspond to any of the studied nine factors. It is possible that compound events of less extreme conditions (e.g. T&P anomalies within 10th-90th percentile) may also lead to extreme events in GPP. These confounding factors may have an impact on the attribution analysis, especially for small events. That may be the reason why there is a slight decrease in overall attribution rate from 95% for 100 events to 92% for 1000 events in TRENDY and from 93% to 87% in Yao-GPP (Fig. 8). And the interpolation to 0.1° from 0.5°-1° spatial-resolution datasets may also introduce uncertainty at pixel scales. Finally, many factors also play important roles in regulating the vulnerability of vegetation GPP to extreme events, for instance different ecosystems (von Buttlar et al., 2018; Xu et al., 2016), management practices (He et al., 2016), and soil conditions (Nepstad et al., 2007). Thus, future studies considering more drivers and regional conditions are necessary to better understand the vulnerability and sensitivity of regional vegetation GPP to extreme events in China. From this, detailed management practice is possible to be carried out to mitigate the damage from future extreme events.

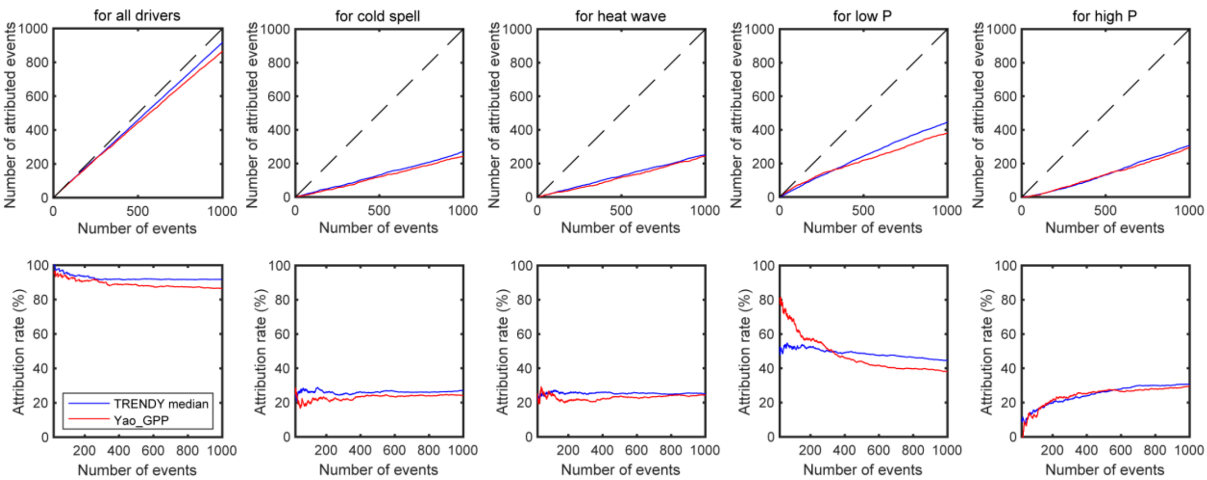


**Fig. 8.** Attribution rate for different number of studied largest GPP events and for each driver.

## 5. Conclusion

In this study, we investigated GPP extreme events in China and sub-regions based on a spatio-temporally contiguous approach using the 5th percentile definition with GPP data from 12 process-based ecosystem models and one observation-based model. Both types of models exhibited that vegetation in Northeast China and North China were most vulnerable to extreme events, especially in mountainous regions. Over the past three decades, 45% and 68% of GPP deficits in China occurred in summer in TRENDY models and Yao-GPP, respectively. Low precipitation was associated with most extreme events among studied nine climatic drivers in China in TRENDY models. Vegetation in southern China is more vulnerable to temperature extremes (i.e. cold spell and heat wave) than in northern China. The importance of cold spells is notable as they have received less attention than droughts in previous studies. Both power law distribution analyses and sensitivity analysis highlight the impacts of drought on large GPP negative anomalies. Our results implied that policymakers could pay more attention to GPP deficits in northern China under drought events and in southern China under temperature extremes in order to mitigate the potential impacts of future climate extremes.


## Acknowledgements

This study was supported by the Natural Science Foundation for Distinguished Young Scholars of Hubei Province of China (2016CFA051), the National Natural Science Foundation of China (No. 41772029 and 41322013), the 111 Project (No. B14031 and B08030). W. Chen acknowledges support from the China Scholarship Council (No. 201806410044) for Ph.D. work at LSCE, France. S. Lienert acknowledges support from the Swiss National Science Foundation (No. 20020_172476).


## References


Arnone, J.A., Verburg, P.S.J., Johnson, D.W., Larsen, J.D., Jasoni, R.L., Lucchesi, A.J., Batts, C.M., von Nagy, C., Coulombe, W.G., Schorran, D.E., Buck, P.E., Braswell, B.H., Coleman, J.S., Sherry, R.A., Wallace, L.L., Luo, Y.Q. and Schimel, D.S., 2008. Prolonged suppression of ecosystem carbon dioxide uptake after an anomalously warm year. Nature, 455(7211): 383-386.

Chen, W., Huang, C., Wang, L. and Li, D., 2018. Climate Extremes and Their Impacts on Interannual Vegetation Variabilities: A Case Study in Hubei Province of Central China. Remote Sens., 10(3): 477.

Chen, Y., Yang, K., He, J., Qin, J., Shi, J., Du, J. and He, Q., 2011. Improving land surface temperature modeling for dry land of China. Journal of Geophysical Research: Atmospheres, 116(D20).

Ciais, P., Reichstein, M., Viovy, N., Granier, A., Ogee, J., Allard, V., Aubinet, M., Buchmann, N., Bernhofer, C., Carrara, A., Chevallier, F., De Noblet, N., Friend, A.D., Friedlingstein, P., Grunwald, T., Heinesch, B., Keronen, P., Knohl, A., Krinner, G., Loustau, D., Manca, G., Matteucci, G., Miglietta, F., Ourcival, J.M., Papale, D., Pilegaard, K., Rambal, S., Seufert, G., Soussana, J.F., Sanz, M.J., Schulze, E.D., Vesala, T. and Valentini, R., 2005. Europe-wide reduction in primary productivity caused by the heat and drought in 2003. Nature, 437(7058): 529-33.

Clauset, A., Shalizi, C.R. and Newman, M.E.J., 2009. Power-Law Distributions in Empirical Data. SIAM Rev., 51(4): 661-703.

Crowther, T.W., Glick, H.B., Covey, K.R., Bettigole, C., Maynard, D.S., Thomas, S.M., Smith, J.R., Hintler, G., Duguid, M.C., Amatulli, G., Tuanmu, M.N., Jetz, W., Salas, C., Stam, C., Piotto, D., Tavani, R., Green, S., Bruce, G., Williams, S.J., Wiser, S.K., Huber, M.O., Hengeveld, G.M., Nabuurs, G.J., Tikhonova, E., Borchardt, P., Li, C.F., Powrie, L.W., Fischer, M., Hemp, A., Homeier, J., Cho, P., Vibrans, A.C., Umunay, P.M., Piao, S.L., Rowe, C.W., Ashton, M.S., Crane, P.R. and Bradford, M.A., 2015. Mapping tree density at a global scale. Nature, 525(7568): 201-5.

Cui, L., Wang, L., Singh, R.P., Lai, Z., Jiang, L. and Yao, R., 2018. Association analysis between spatiotemporal variation of vegetation greenness and precipitation/temperature in the Yangtze River Basin (China). Environ. Sci. Pollut. Res.: 1-12.

Du, L., Mikle, N., Zou, Z., Huang, Y., Shi, Z., Jiang, L., McCarthy, H.R., Liang, J. and Luo, Y., 2018. Global patterns of extreme drought-induced loss in land primary production: Identifying ecological extremes from rain-use efficiency. Sci. Total Environ., 628-629: 611-620.

Felton, A.J. and Smith, M.D., 2017. Integrating plant ecological responses to climate extremes from individual to ecosystem levels. Philos Trans R Soc Lond B Biol Sci, 372(1723).

Frank, D., Reichstein, M., Bahn, M., Thonicke, K., Frank, D., Mahecha, M.D., Smith, P., van der Velde, M., Vicca, S., Babst, F., Beer, C., Buchmann, N., Canadell, J.G., Ciais, P., Cramer, W., Ibrom, A., Miglietta, F., Poulter, B., Rammig, A., Seneviratne, S.I., Walz, A., Wattenbach, M., Zavala, M.A. and Zscheischler, J., 2015. Effects of climate extremes on the terrestrial carbon cycle: concepts, processes and potential future impacts. Glob Chang Biol, 21(8): 2861-80.

Ge, J., Xiong, G., Wang, Z., Zhang, M., Zhao, C., Shen, G., Xu, W. and Xie, Z., 2015. Altered dynamics of broad-leaved tree species in a Chinese subtropical montane mixed forest: the role of an anomalous extreme 2008 ice storm episode. Ecol Evol, 5(7): 1484-93.

Guimberteau, M., Zhu, D., Maignan, F., Huang, Y., Yue, C., Dantec-Nédélec, S., Ottlé, C., Jornet-Puig, A., Bastos, A., Laurent, P., Goll, D., Bowring, S., Chang, J., Guenet, B., Tifafi, M., Peng, S., Krinner, G., Ducharne, A., Wang, F., Wang, T., Wang, X., Wang, Y., Yin, Z., Lauerwald, R., Joetzjer, E., Qiu, C., Kim, H. and Ciais, P., 2018. ORCHIDEE-MICT (v8.4.1), a land surface model for the high latitudes: model description and validation. Geosci. Model Dev., 11(1): 121-163.

Hantson, S., Pueyo, S. and Chuvieco, E., 2015. Global fire size distribution is driven by human impact and climate. Global Ecol. Biogeogr., 24(1): 77-86.

Hao, Y.B., Zhou, C.T., Liu, W.J., Li, L.F., Kang, X.M., Jiang, L.L., Cui, X.Y., Wang, Y.F., Zhou, X.Q. and Xu, C.Y., 2017. Aboveground net primary productivity and carbon balance remain stable under extreme precipitation events in a semiarid steppe ecosystem. Agric. For. Meteorol., 240: 1-9.

Harris, I., Jones, P., Osborn, T. and Lister, D., 2014. Updated high - resolution grids of monthly climatic observations - the CRU TS3. 10 Dataset. Int. J. Climatol., 34(3): 623-642.

Haverd, V., Smith, B., Nieradzik, L., Briggs, P., Woodgate, W., Trudinger, C. and Canadell, J., 2017. A new version of the CABLE land surface model (Subversion revision r4546), incorporating land use and land cover change, woody vegetation demography and a novel optimisation-based approach to plant coordination of electron transport and carboxylation capacity-limited photosynthesis, Geosci. Model Dev. Discuss.

He, S.Y., Richards, K. and Zhao, Z.Q., 2016. Climate extremes in the Kobresia meadow area of the Qinghai-Tibetan Plateau, 1961-2008. Environmental Earth Sciences, 75(1): 15.

Huang, Y., Gerber, S., Huang, T. and Lichstein, J.W., 2016. Evaluating the drought response of CMIP5 models using global gross primary productivity, leaf area, precipitation, and soil moisture data. Global Biogeochem. Cycles, 30(12): 1827-1846.

IPCC, 2012. Managing the Risks of Extreme Events and Disasters to Advance Climate Change Adaption. Cambridge University Press, Cambridge, UK.

IPCC, 2013. Climate Change 2013: The Physical Science Basis. Contribution of Working Group I to the Fifth Assessment Report of the Intergovernmental Panel on Climate Change. Cambridge University Press, Cambridge, UK; New York, NY, USA, 1535 pp.

Isbell, F., Craven, D., Connolly, J., Loreau, M., Schmid, B., Beierkuhnlein, C., Bezemer, T.M., Bonin, C., Bruelheide, H., de Luca, E., Ebeling, A., Griffin, J.N., Guo, Q., Hautier, Y., Hector, A., Jentsch, A., Kreyling, J., Lanta, V., Manning, P., Meyer, S.T., Mori, A.S., Naeem, S., Niklaus, P.A., Polley, H.W., Reich, P.B., Roscher, C., Seabloom, E.W., Smith, M.D., Thakur, M.P., Tilman, D., Tracy, B.F., van der Putten, W.H., van Ruijven, J., Weigelt, A., Weisser, W.W., Wilsey, B. and Eisenhauer, N., 2015. Biodiversity increases the resistance of ecosystem productivity to climate extremes. Nature, 526(7574):

574-7.

Jain, A.K., Meiyappan, P., Song, Y. and House, J.I., 2013. CO2 emissions from land-use change affected more by nitrogen cycle, than by the choice of land-cover data. Global Change Biol., 19(9): 2893-2906.

Jung, M., Reichstein, M., Margolis, H.A., Cescatti, A., Richardson, A.D., Arain, M.A., Arneth, A., Bernhofer, C., Bonal, D. and Chen, J., 2011. Global patterns of land‐atmosphere fluxes of carbon dioxide, latent heat, and sensible heat derived from eddy covariance, satellite, and meteorological observations. J. Geophys. Res., 116(G3): 245-255.

Kato, E., Kinoshita, T., Ito, A., Kawamiya, M. and Yamagata, Y., 2013. Evaluation of spatially explicit emission scenario of land-use change and biomass burning using a process-based biogeochemical model. Journal of Land Use Science, 8(1): 104-122.

Keller, K.M., Lienert, S., Bozbiyik, A., Stocker, T.F., Churakova, O.V., Frank, D.C., Klesse, S., Koven, C.D., Leuenberger, M., Riley, W.J., Saurer, M., Siegwolf, R., Weigt, R.B. and Joos, F., 2017. 20th century changes in carbon isotopes and water-use efficiency: tree-ring-based evaluation of the CLM4.5 and LPX-Bern models. Biogeosciences, 14(10): 2641-2673.

Krinner, G., Viovy, N., de Noblet-Ducoudre, N., Ogee, J., Polcher, J., Friedlingstein, P., Ciais, P., Sitch, S. and Prentice, I.C., 2005. A dynamic global vegetation model for studies of the coupled atmosphere-biosphere system. Global Biogeochem. Cycles, 19(1).

Le Quéré, C.A., Robbie M, Friedlingstein, P., Sitch, S., Pongratz, J., Manning, A.C., Korsbakken, J.I., Peters, G.P., Canadell, J.G. and Jackson, R.B., 2018. Global Carbon Budget 2017. Earth Syst. Sci. Data, 10(1): 405-448.

Lesk, C., Rowhani, P. and Ramankutty, N., 2016. Influence of extreme weather disasters on global crop production. Nature, 529(7584): 84-7.

Liu, Q., Piao, S., Janssens, I.A., Fu, Y., Peng, S., Lian, X., Ciais, P., Myneni, R.B., Penuelas, J. and Wang, T., 2018. Extension of the growing season increases vegetation exposure to frost. Nat. Commun., 9(1): 426.

Lloyd‐Hughes, B., 2012. A spatio‐temporal structure‐based approach to drought characterisation. Int. J. Climatol., 32(3): 406-418.

Lobell, D.B., Sibley, A. and Ortiz-Monasterio, J.I., 2012. Extreme heat effects on wheat senescence in India. Nat. Clim. Change, 2(3): 186-189.

Lombardozzi, D.L., Bonan, G.B., Smith, N.G., Dukes, J.S. and Fisher, R.A., 2015. Temperature acclimation of photosynthesis and respiration: A key uncertainty in the carbon cycle‐climate feedback. Geophys. Res. Lett., 42(20): 8624-8631.

Los, S.O., 2013. Analysis of trends in fused AVHRR and MODIS NDVI data for 1982–2006: Indication for a CO2 fertilization effect in global vegetation. Global Biogeochem. Cycles, 27(2): 318–330.

Nepstad, D.C., Tohver, I.M., Ray, D., Moutinho, P. and Cardinot, G., 2007. Mortality of large trees and lianas following experimental drought in an amazon forest. Ecology, 88(9): 2259-2269.

Niu, X., Wang, S., Tang, J., Lee, D.K., Gutowski, W., Dairaku, K., McGregor, J., Katzfey, J., Gao, X. and Wu, J., 2017. Ensemble evaluation and projection of climate extremes in China using RMIP models. Int. J. Climatol., 38(4): 2039-2055.

Oleson, K., Lawrence, M., Bonan, B., Drewniak, B., Huang, M., Koven, D., Levis, S., Li, F., Riley, J. and Subin, M., 2013. Technical description of version 4.5 of the Community Land Model (CLM).

Piao, S., Ciais, P., Huang, Y., Shen, Z., Peng, S., Li, J., Zhou, L., Liu, H., Ma, Y., Ding, Y., Friedlingstein, P., Liu, C., Tan, K., Yu, Y., Zhang, T. and Fang, J., 2010. The impacts of climate change on water resources and agriculture in China. Nature, 467(7311): 43-51.

Piao, S., Sitch, S., Ciais, P., Friedlingstein, P., Peylin, P., Wang, X., Ahlstrom, A., Anav, A., Canadell, J.G., Cong, N., Huntingford, C., Jung, M., Levis, S., Levy, P.E., Li, J., Lin, X., Lomas, M.R., Lu, M., Luo, Y., Ma, Y., Myneni, R.B., Poulter, B., Sun, Z., Wang, T., Viovy, N., Zaehle, S. and Zeng, N., 2013. Evaluation of terrestrial carbon cycle models for their response to climate variability and to CO2 trends. Glob Chang Biol, 19(7): 2117-32.

Randerson, J.T., van der Werf, G.R., Giglio, L., Collatz, G.J. and Kasibhatla, P.S., 2017. Global Fire Emissions Database, Version 4.1 (GFEDv4). Global Fire Emissions Database, Version 4.1 (GFEDv4). ORNL DAAC, Oak Ridge, Tennessee, USA.

Reichstein, M., Bahn, M., Ciais, P., Frank, D., Mahecha, M.D., Seneviratne, S.I., Zscheischler, J., Beer, C., Buchmann, N., Frank, D.C., Papale, D., Rammig, A., Smith, P., Thonicke, K., van der Velde, M., Vicca, S., Walz, A. and Wattenbach, M., 2013. Climate extremes and the carbon cycle. Nature, 500(7462): 287-95.

Ren, W., Tian, H.Q., Tao, B., Huang, Y. and Pan, S.F., 2012. China's crop productivity and soil carbon storage as influenced by multifactor global change. Global Change Biol., 18(9): 2945-2957.

Samaniego, L., Thober, S., Kumar, R., Wanders, N., Rakovec, O., Pan, M., Zink, M., Sheffield, J., Wood, E.F. and Marx, A., 2018. Anthropogenic warming exacerbates European soil moisture droughts. Nat. Clim. Change, 8(5): 421-426.

Scannell, H.A., Pershing, A.J., Alexander, M.A., Thomas, A.C. and Mills, K.E., 2016. Frequency of marine heatwaves in the North Atlantic and North Pacific since 1950. Geophys. Res. Lett., 43(5): 2069-2076.

Schwalm, C.R., Anderegg, W.R.L., Michalak, A.M., Fisher, J.B., Biondi, F., Koch, G., Litvak, M., Ogle, K., Shaw, J.D., Wolf, A., Huntzinger, D.N., Schaefer, K., Cook, R., Wei, Y., Fang, Y., Hayes, D., Huang, M., Jain, A. and Tian, H., 2017. Global patterns of drought recovery. Nature, 548(7666): 202-205.

Shi, J., Cui, L., Wen, K., Tian, Z., Wei, P. and Zhang, B., 2018. Trends in the consecutive days of temperature and precipitation extremes in China during 1961-2015. Environ. Res., 161: 381-391.

Sitch, S., Friedlingstein, P., Gruber, N., Jones, S.D., Murray-Tortarolo, G., Ahlstrom, A., Doney, S.C., Graven, H., Heinze, C., Huntingford, C., Levis, S., Levy, P.E., Lomas, M., Poulter, B., Viovy, N., Zaehle, S., Zeng, N., Arneth, A., Bonan, G., Bopp, L., Canadell, J.G., Chevallier, F., Ciais, P., Ellis, R., Gloor, M., Peylin, P., Piao, S.L., Le Quere, C., Smith, B., Zhu, Z. and Myneni, R., 2015. Recent trends and drivers of regional sources and sinks of carbon dioxide. Biogeosciences, 12(3): 653-679.

Sitch, S., Smith, B., Prentice, I.C., Arneth, A., Bondeau, A., Cramer, W., Kaplan, J.O., Levis, S., Lucht, W., Sykes, M.T., Thonicke, K. and Venevsky, S., 2003. Evaluation of ecosystem dynamics, plant geography and terrestrial carbon cycling in the LPJ dynamic global vegetation model. Global Change Biol., 9(2): 161-185.

Smith, B., Warlind, D., Arneth, A., Hickler, T., Leadley, P., Siltberg, J. and Zaehle, S., 2014. Implications of incorporating N cycling and N limitations on primary production in an individual-based dynamic vegetation model. Biogeosciences, 11(7): 2027-2054.

Sui, Y., Lang, X. and Jiang, D., 2018. Projected signals in climate extremes over China associated with a 2 °C global warming under two RCP scenarios. Int. J. Climatol., 38(S1): e678-e697.

Teuling, A.J., Seneviratne, S.I., Stockli, R., Reichstein, M., Moors, E., Ciais, P., Luyssaert, S., van den Hurk, B., Ammann, C., Bernhofer, C., Dellwik, E., Gianelle, D., Gielen, B., Grunwald, T., Klumpp, K., Montagnani, L., Moureaux, C., Sottocornola, M. and Wohlfahrt, G., 2010. Contrasting response of

European forest and grassland energy exchange to heatwaves. Nat. Geosci., 3(10): 722-727.

Tian, H., Ren, W., Tao, B., Sun, G., Chappelka, A., Wang, X., Pan, S., Yang, J., Liu, J. and S. Felzer, B., 2016. Climate extremes and ozone pollution: a growing threat to China's food security. Ecosyst. Health Sustainability, 2(1): e01203.

Tian, H.Q., Chen, G.S., Lu, C.Q., Xu, X.F., Hayes, D.J., Ren, W., Pan, S.F., Huntzinger, D.N. and Wofsy, S.C., 2015. North American terrestrial CO2 uptake largely offset by CH4 and N2O emissions: toward a full accounting of the greenhouse gas budget. Clim. Change, 129(3-4): 413-426.

van der Schrier, G., Barichivich, J., Briffa, K.R. and Jones, P.D., 2013. A scPDSI-based global data set of dry and wet spells for 1901-2009. Journal of Geophysical Research: Atmospheres, 118(10): 4025-4048.

von Buttlar, J., Zscheischler, J., Rammig, A., Sippel, S., Reichstein, M., Knohl, A., Jung, M., Menzer, O., Arain, M.A., Buchmann, N., Cescatti, A., Gianelle, D., Kiely, G., Law, B.E., Magliulo, V., Margolis, H., McCaughey, H., Merbold, L., Migliavacca, M., Montagnani, L., Oechel, W., Pavelka, M., Peichl, M., Rambal, S., Raschi, A., Scott, R.L., Vaccari, F.P., van Gorsel, E., Varlagin, A., Wohlfahrt, G. and Mahecha, M.D., 2018. Impacts of droughts and extreme-temperature events on gross primary production and ecosystem respiration: a systematic assessment across ecosystems and climate zones. Biogeosciences, 15(5): 1293-1318.

Wang, L., Zhu, H., Lin, A., Zou, L., Qin, W. and Du, Q., 2017. Evaluation of the Latest MODIS GPP Products across Multiple Biomes Using Global Eddy Covariance Flux Data. Remote Sens., 9(5): 418.

Woodward, F.I., Smith, T.M. and Emanuel, W.R., 1995. A global land primary productivity and phytogeography model. Global Biogeochem. Cycles, 9(4): 471-490.

Xu, X.T., Piao, S.L., Wang, X.H., Chen, A.P., Ciais, P. and Myneni, R.B., 2012. Spatio-temporal patterns of the area experiencing negative vegetation growth anomalies in China over the last three decades. Environ. Res. Lett., 7(3): 9.

Xu, Y., Shen, Z.H., Ying, L.X., Ciais, P., Liu, H.Y., Piao, S.L., Wen, C. and Jiang, Y.X., 2016. The exposure, sensitivity and vulnerability of natural vegetation in China to climate thermal variability (1901-2013): An indicator-based approach. Ecol. Indic., 63: 258-272.

Yao, J., Chen, Y., Zhao, Y., Mao, W., Xu, X., Liu, Y. and Yang, Q., 2017. Response of vegetation NDVI to climatic extremes in the arid region of Central Asia: a case study in Xinjiang, China. Theor. Appl. Climatol.: 1-13.

Yao, R., Wang, L., Huang, X., Chen, X. and Liu, Z., 2019. Increased spatial heterogeneity in vegetation greenness due to vegetation greening in mainland China. Ecol. Indic., 99: 240-250.

Yao, Y., Wang, X., Li, Y., Wang, T., Shen, M., Du, M., He, H., Li, Y., Luo, W., Ma, M., Ma, Y., Tang, Y., Wang, H., Zhang, X., Zhang, Y., Zhao, L., Zhou, G. and Piao, S., 2018. Spatiotemporal pattern of gross primary productivity and its covariation with climate in China over the last thirty years. Glob Chang Biol, 24(1): 184-196.

Yuan, W., Cai, W., Chen, Y., Liu, S., Dong, W., Zhang, H., Yu, G., Chen, Z., He, H., Guo, W., Liu, D., Liu, S., Xiang, W., Xie, Z., Zhao, Z. and Zhou, G., 2016. Severe summer heatwave and drought strongly reduced carbon uptake in Southern China. Sci. Rep., 6: 18813.

Yuan, W.P., Liu, D., Dong, W.J., Liu, S.G., Zhou, G.S., Yu, G.R., Zhao, T.B., Feng, J.M., Ma, Z.G., Chen, J.Q., Chen, Y., Chen, S.P., Han, S.J., Huang, J.P., Li, L.H., Liu, H.Z., Liu, S.M., Ma, M.G., Wang, Y.F., Xia, J.Z., Xu, W.F., Zhang, Q., Zhao, X.Q. and Zhao, L., 2014. Multiyear precipitation reduction strongly decreases carbon uptake over northern China. J. Geophys. Res. Biogeosci., 119(5): 881-896.

Zeng, N., Mariotti, A. and Wetzel, P., 2005. Terrestrial mechanisms of interannual CO(2) variability. Global Biogeochem. Cycles, 19(1).

Zhang, L., Xiao, J.F., Li, J., Wang, K., Lei, L.P. and Guo, H.D., 2012. The 2010 spring drought reduced primary productivity in southwestern China. Environ. Res. Lett., 7(4): 045706.

Zhu, Z.C., Piao, S.L., Myneni, R.B., Huang, M.T., Zeng, Z.Z., Canadell, J.G., Ciais, P., Sitch, S., Friedlingstein, P., Arneth, A., Cao, C.X., Cheng, L., Kato, E., Koven, C., Li, Y., Lian, X., Liu, Y.W., Liu, R.G., Mao, J.F., Pan, Y.Z., Peng, S.S., Penuelas, J., Poulter, B., Pugh, T.A.M., Stocker, B.D., Viovy, N., Wang, X.H., Wang, Y.P., Xiao, Z.Q., Yang, H., Zaehle, S. and Zeng, N., 2016. Greening of the Earth and its drivers. Nat. Clim. Change, 6(8): 791-795.

Zscheischler, J., Mahecha, M.D., Harmeling, S. and Reichstein, M., 2013. Detection and attribution of large spatiotemporal extreme events in Earth observation data. Ecol. Inf., 15: 66-73.

Zscheischler, J., Mahecha, M.D., von Buttlar, J., Harmeling, S., Jung, M., Rammig, A., Randerson, J.T., Scholkopf, B., Seneviratne, S.I., Tomelleri, E., Zaehle, S. and Reichstein, M., 2014a. A few extreme events dominate global interannual variability in gross primary production. Environ. Res. Lett., 9(3): 035001.

Zscheischler, J., Michalak, A.M., Schwalm, C., Mahecha, M.D., Huntzinger, D.N., Reichstein, M., Berthier, G., Ciais, P., Cook, R.B., El-Masri, B., Huang, M., Ito, A., Jain, A., King, A., Lei, H., Lu, C., Mao, J., Peng, S., Poulter, B., Ricciuto, D., Shi, X., Tao, B., Tian, H., Viovy, N., Wang, W., Wei, Y., Yang, J. and Zeng, N., 2014b. Impact of large-scale climate extremes on biospheric carbon fluxes: An intercomparison based on MsTMIP data. Global Biogeochem. Cycles, 28(6): 585-600.

Zscheischler, J., Reichstein, M., Harmeling, S., Rammig, A., Tomelleri, E. and Mahecha, M.D., 2014c. Extreme events in gross primary production: a characterization across continents. Biogeosciences, 11(11): 2909-2924.

Zscheischler, J., Reichstein, M., von Buttlar, J., Mu, M., Randerson, J.T. and Mahecha, M.D., 2014d. Carbon cycle extremes during the 21st century in CMIP5 models: Future evolution and attribution to climatic drivers. Geophys. Res. Lett., 41(24): 8853-8861.

Zscheischler, J., Westra, S., van den Hurk, B.J.J.M., Seneviratne, S.I., Ward, P.J., Pitman, A., AghaKouchak, A., Bresch, D.N., Leonard, M., Wahl, T. and Zhang, X., 2018. Future climate risk from compound events. Nat. Clim. Change, 8(6): 469-477.

## Appendices

## Figure Legends

**Fig. A.1** The spatial distributions of (a, b) mean annual temperature and (c, d) mean annual precipitation for the period of 1982-2015 with (a, c) CRU and (b, d) ITPCAS data. The blue line in panel (d) denotes the 800-mm annual precipitation line of China, which separates China into northern and southern China.

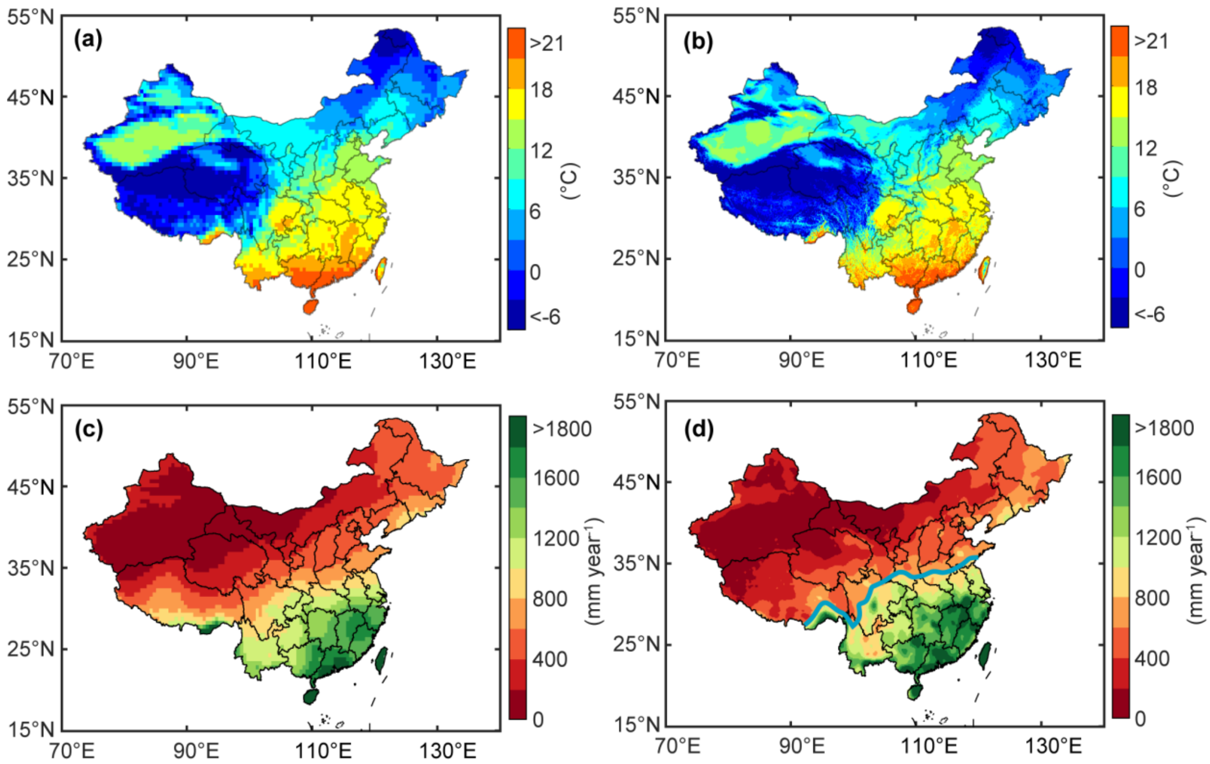

**Fig. A.2** The distribution of duration of the 1000 largest negative extreme events for each GPP data.

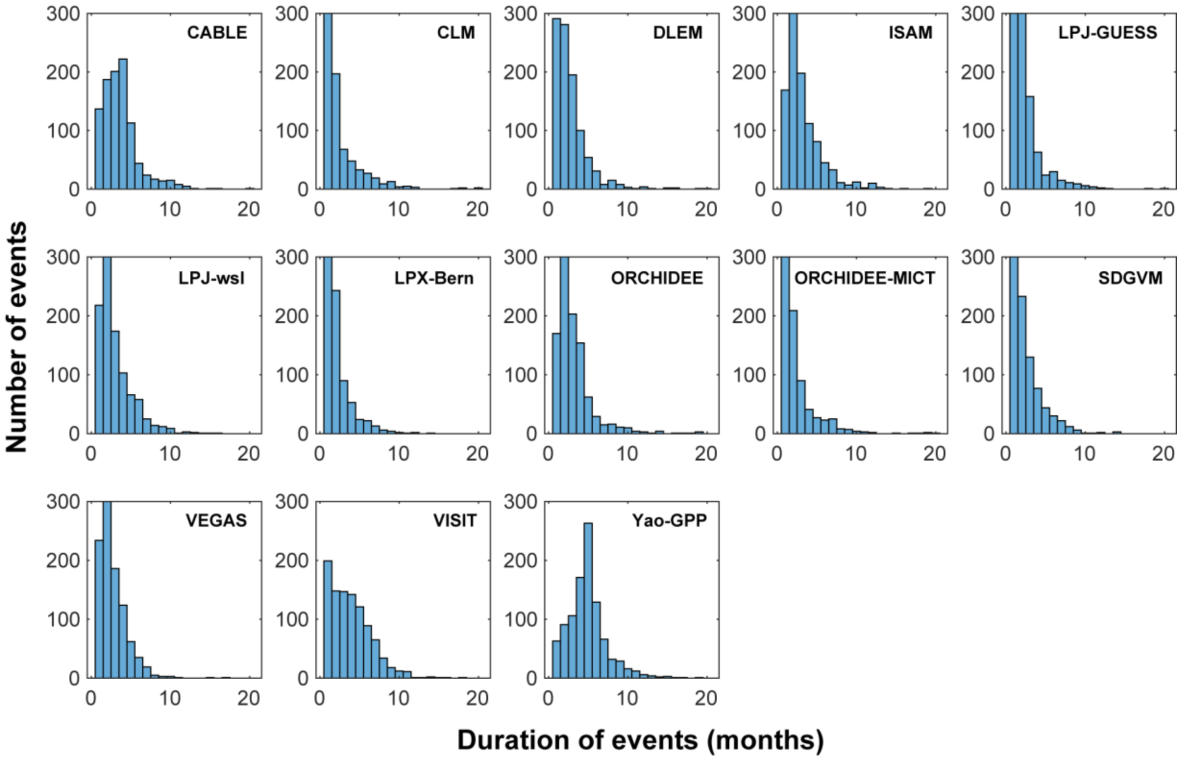

**Fig. A.3** The spatial distributions of negative extreme events in GPP during 1982-2015 for the 12 process-based TRENDY models. The 1000 largest negative extreme events were calculated using the 5th percentile definition. White areas indicate no data.

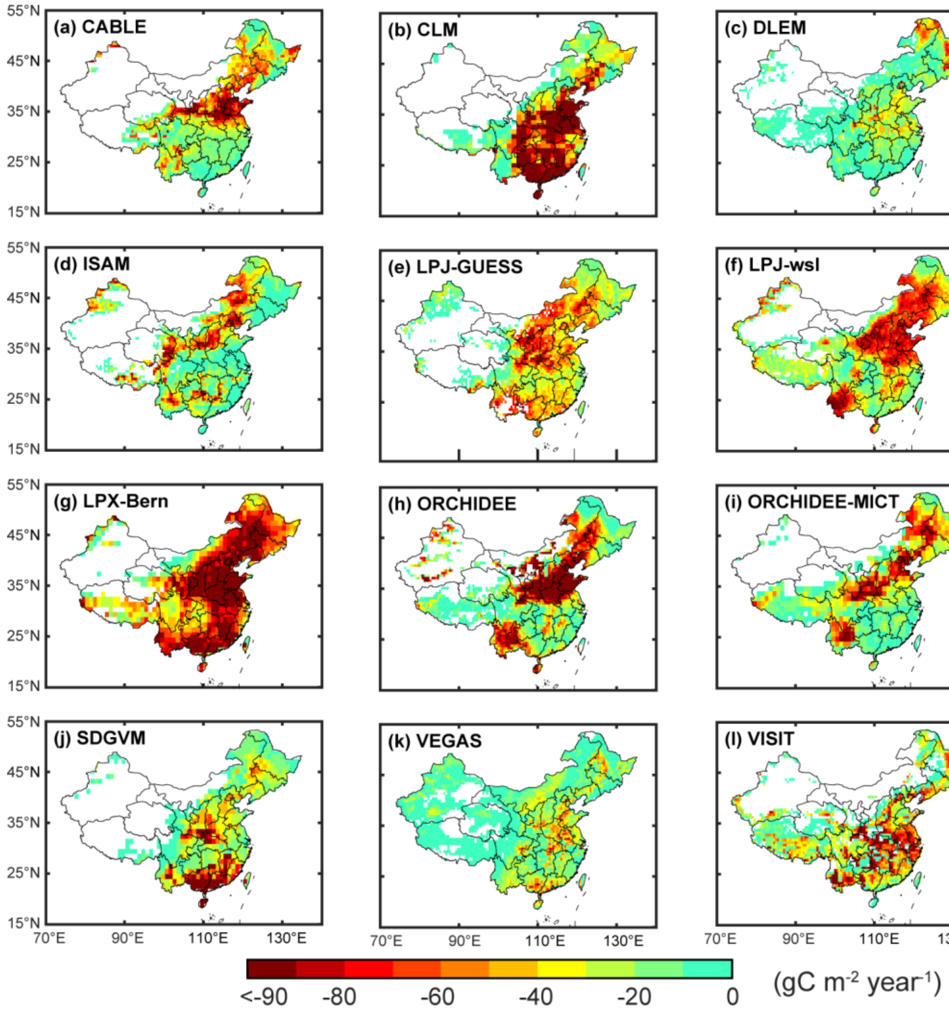

**Fig. A.4** The bar graph to show the attribution of the 1000 largest extreme events in China for each model.

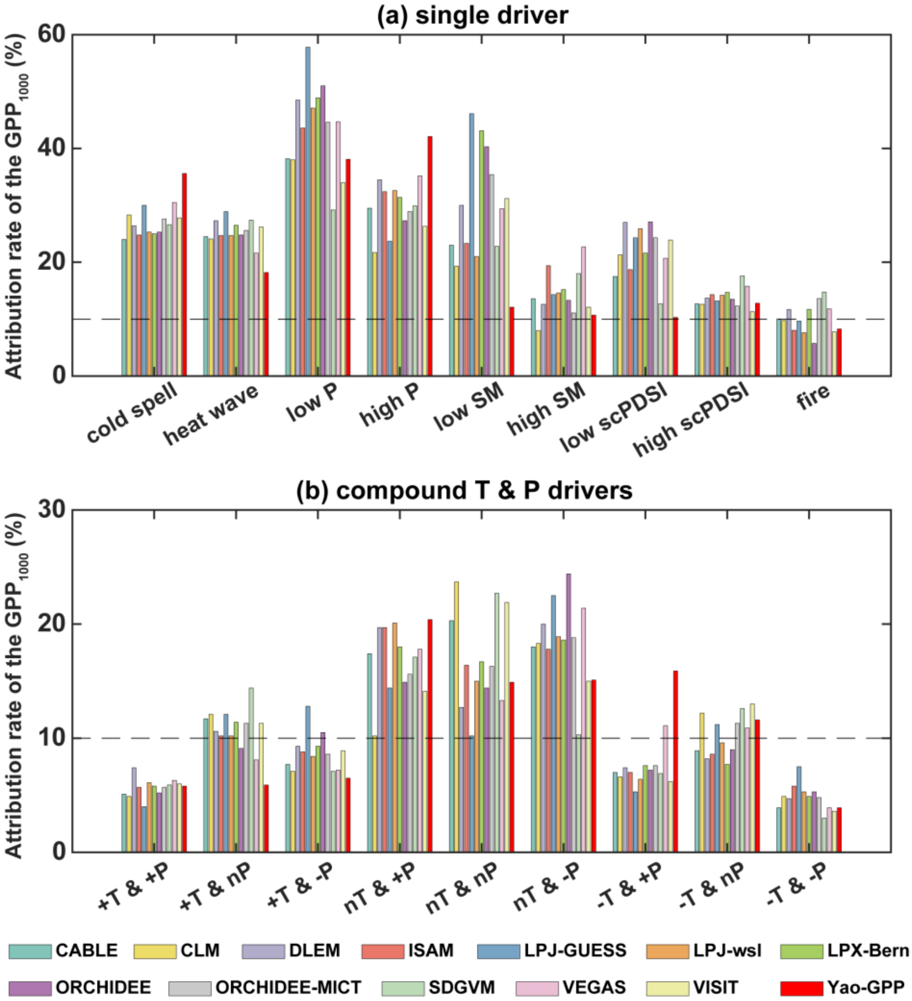

840 **Fig. A.5** Attribution rate of GPP extreme events to compound T&P effects for the nine sub-
841 regions of China. The largest 100 negative extreme events were used for each sub-region.
842

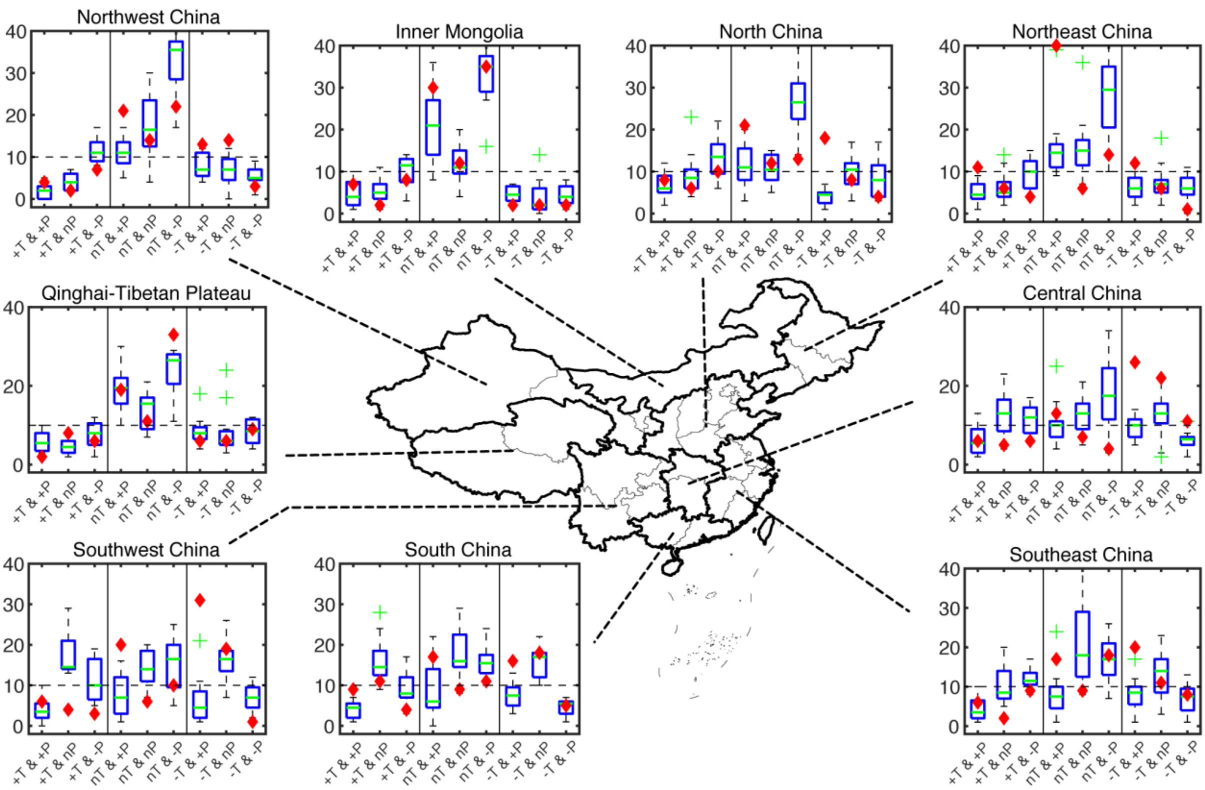


843

**Fig. A.6** The probability distributions of sizes of extreme events for the nine sub-regions of China. The color legend to distinguish datasets is the same as Fig. 2. The letter $\alpha_m$ and $\alpha_Y$ are median of the fitted exponents over the 12 process-based models and exponent for Yao-GPP, respectively. The power law fitting and goodness-of-fit parameters are presented in Table A.3. The color legend to distinguish GPP datasets is the same as Fig. A.4.

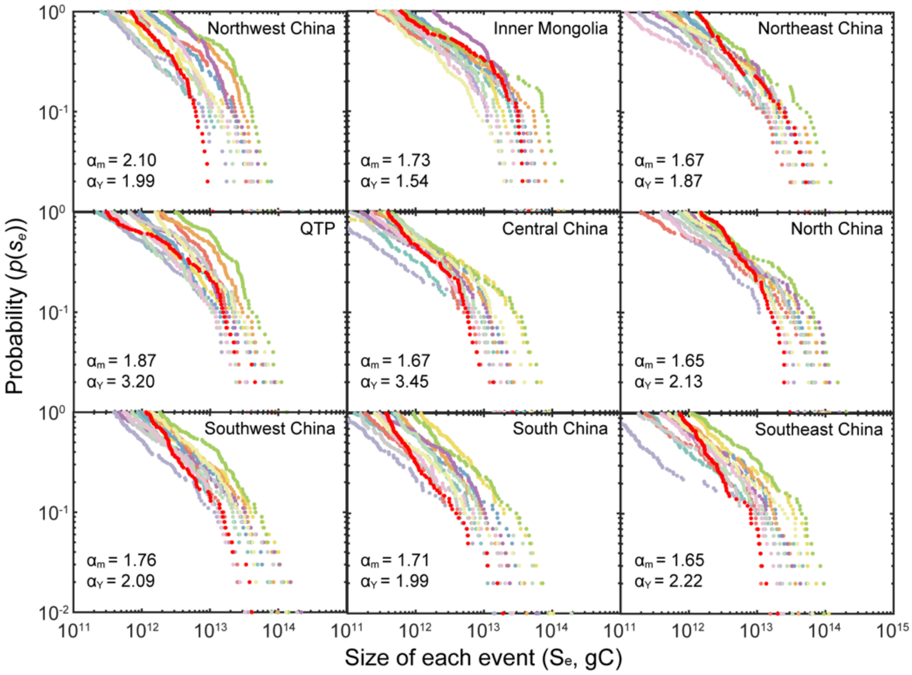

**Fig. A.7** Attribution rate for different number of studied largest GPP events and for different drivers.

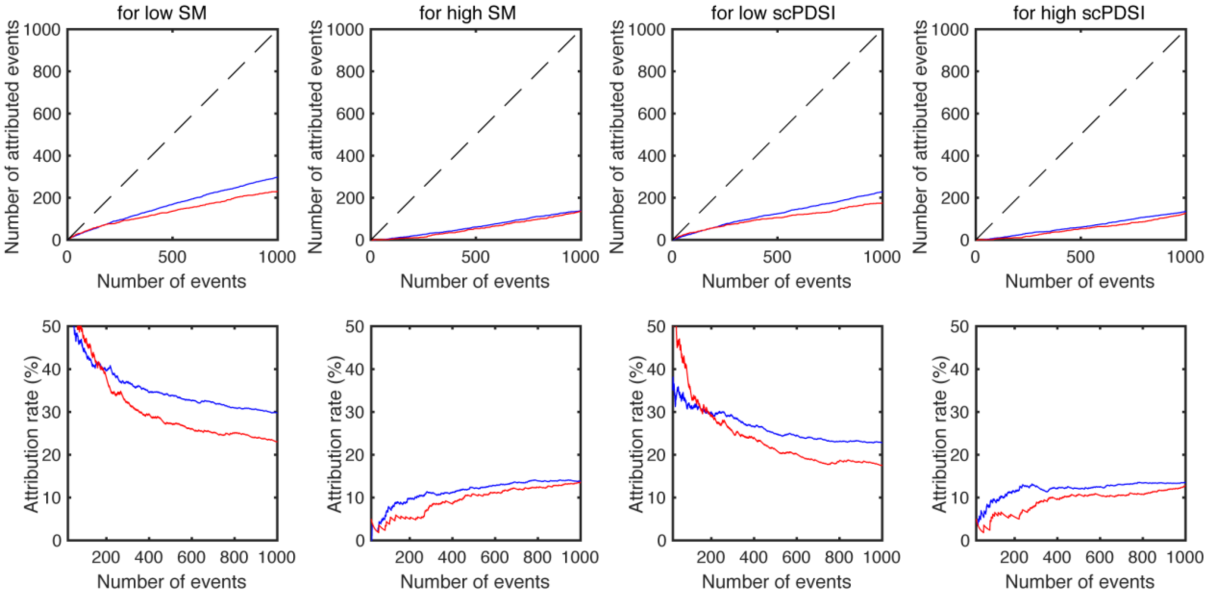

## Tables

**Table A.1** Information on the 12 process-based TRENDY models used in this study.

| Model | Long name | Spatial Resolution | Reference |
|---|---|---|---|
| CABLE | The CSIRO Atmosphere Biosphere Land Exchange Model | 0.5° × 0.5° | (Haverd et al., 2017) |
| CLM4.5 | Community Land Model version 4.5 | 0.9375°× 1.25° | (Oleson et al., 2013) |
| DLEM | Dynamic Land Ecosystem Model | 0.5° × 0.5° | (Tian et al., 2015) |
| ISAM | Integrated Science Assessment Model | 0.5° × 0.5° | (Jain et al., 2013) |
| LPJ-GUESS | Lund-Potsdam-Jena Dynamic Global Vegetation Model | 0.5° × 0.5° | (Smith et al., 2014) |
| LPJ-wsl | Lund-Potsdam-Jena Dynamic Global Vegetation Model | 0.5° × 0.5° | (Sitch et al., 2003) |
| LPX-Bern | Land surface Processes and eXchanges version 1.3 | 1° × 1° | (Keller et al., 2017) |
| ORCHIDEE | Organizing Carbon and Hydrology in Dynamic Ecosystems Land Surface Model | 0.5° × 0.5° | (Krinner et al., 2005) |
| ORCHIDEE-MICT | Organizing Carbon and Hydrology in Dynamic Ecosystems Land Surface Model | 1° × 1° | (Guimberteau et al., 2018) |
| SDGVM | Sheffield Dynamic Global Vegetation Model | 1° × 1° | (Woodward et al., 1995) |
| VEGAS | Vegetation Global Atmosphere Soils | 0.5° × 0.5° | (Zeng et al., 2005) |
| VISIT | Vegetation Integrative Simulator for Trace Gases | 0.5° × 0.5° | (Kato et al., 2013) |

**Table A.2** The power-law fits and the corresponding p-values for extreme events induced by different drivers in Fig. 6. The letters of 'n', 'a' and 'p' denote the sample size, the exponent of the fitted power law and p-value, respectively. The statistically significant values where p-value > 0.1 are denoted in bold.

| | Cold spell | | | Heat wave | | | Low P | | | High P | | | Low SM | | | High SM | | | Low scPDSI | | | High scPDSI | | | Fire | | |
|---|---|---|---|---|---|---|---|---|---|---|---|---|---|---|---|---|---|---|---|---|---|---|---|---|---|---|---|
| | n | a | p | n | a | p | n | a | p | n | a | p | n | a | p | n | a | p | n | a | p | n | a | p | n | a | p |
| CABLE | 240 | 1.70 | **0.86** | 245 | 1.67 | **0.92** | 382 | 1.51 | 0.06 | 295 | 2.10 | **0.39** | 175 | 1.47 | **0.36** | 127 | 1.87 | 0.05 | 196 | 1.49 | **0.79** | 146 | 2.17 | **0.12** | 56 | 2.06 | **0.97** |
| CLM4.5 | 283 | 1.89 | **0.10** | 241 | 1.74 | 0.06 | 380 | 1.67 | **0.22** | 217 | 1.97 | **0.44** | 213 | 1.71 | **0.15** | 126 | 2.16 | **0.27** | 256 | 1.46 | **0.61** | 118 | 2.05 | **0.69** | 52 | 2.16 | **0.18** |
| DLEM | 264 | 1.66 | **0.91** | 273 | 1.74 | **0.48** | 485 | 1.73 | **0.43** | 345 | 1.72 | **0.45** | 270 | 1.76 | **0.86** | 137 | 1.67 | 0.02 | 297 | 1.66 | 0.02 | 149 | 1.78 | **0.40** | 72 | 3.05 | **0.89** |
| ISAM | 248 | 1.55 | 0.04 | 247 | 1.61 | **0.17** | 436 | 1.53 | 0.02 | 324 | 1.81 | **0.35** | 187 | 1.54 | 0 | 143 | 1.70 | **0.25** | 181 | 1.56 | 0.01 | 159 | 1.74 | **0.63** | 44 | 2.09 | **0.78** |
| LPJ-GUESS | 300 | 1.80 | **0.78** | 289 | 1.74 | **0.77** | 578 | 1.61 | **0.25** | 237 | 1.87 | **0.95** | 243 | 1.53 | **0.49** | 132 | 1.89 | **0.50** | 257 | 1.52 | **0.22** | 127 | 1.78 | **0.99** | 55 | 2.19 | **0.83** |
| LPJ-wsl | 253 | 1.66 | 0.04 | 247 | 1.57 | **0.67** | 471 | 1.55 | 0.06 | 326 | 1.92 | **0.59** | 259 | 1.52 | **0.31** | 142 | 1.75 | 0.05 | 229 | 1.52 | 0 | 165 | 1.92 | 0.02 | 39 | 2.51 | **0.81** |
| LPX-Bern | 250 | 1.72 | **0.21** | 265 | 1.77 | **0.90** | 489 | 1.65 | **0.36** | 314 | 1.87 | **0.95** | 216 | 1.72 | **0.75** | 147 | 1.80 | **0.86** | 221 | 1.48 | **0.11** | 146 | 1.85 | **0.47** | 65 | 2.15 | **0.71** |
| ORCHIDEE | 253 | 1.70 | **0.80** | 248 | 1.65 | **0.47** | 510 | 1.63 | **0.14** | 273 | 2.18 | **0.91** | 271 | 1.50 | 0.06 | 135 | 2.15 | **0.54** | 277 | 1.55 | **0.44** | 145 | 2.15 | **0.16** | 31 | 2.63 | 0.08 |
| ORCHIDEE-MICT | 276 | 1.65 | **0.78** | 256 | 1.70 | **0.74** | 446 | 1.51 | 0.03 | 289 | 1.80 | **0.75** | 243 | 1.51 | 0.06 | 123 | 1.86 | **0.92** | 243 | 1.40 | 0.06 | 117 | 1.94 | **0.85** | 72 | 2.17 | **0.10** |
| SDGVM | 266 | 1.75 | **0.32** | 274 | 1.76 | 0.03 | 292 | 1.70 | **0.76** | 299 | 1.82 | **0.93** | 127 | 1.66 | **0.20** | 176 | 1.70 | 0.01 | 168 | 1.68 | **0.60** | 192 | 1.82 | **0.80** | 87 | 2.59 | **0.93** |
| VEGAS | 305 | 1.55 | **0.24** | 216 | 1.56 | 0 | 447 | 1.60 | 0.04 | 352 | 1.65 | 0.03 | 207 | 1.51 | 0 | 158 | 1.68 | **0.64** | 220 | 1.50 | 0.02 | 167 | 1.70 | **0.45** | 65 | 2.10 | **0.50** |
| VISIT | 278 | 1.59 | 0.02 | 262 | 1.69 | **0.75** | 340 | 1.60 | **0.59** | 263 | 1.83 | **0.63** | 239 | 1.53 | **0.51** | 113 | 1.75 | **0.26** | 237 | 1.54 | **0.14** | 120 | 1.75 | **0.60** | 42 | 2.23 | **0.29** |
| Yao-GPP | 356 | 1.87 | 0 | 182 | 1.75 | **0.43** | 381 | 1.84 | **0.44** | 421 | 1.71 | 0.01 | 103 | 2.09 | **0.96** | 128 | 2.18 | **0.93** | 123 | 2.18 | **0.28** | 116 | 2.22 | 0.06 | 46 | 2.23 | **0.78** |

**Table A.3** The power-law fits and the corresponding p-values for extreme events in different sub-regions in Fig. A.3. The letters of 'n', 'a' and 'p' denote the sample size, the exponent of the fitted power law and p-value, respectively. The statistically significant values where p-value > 0.1 are denoted in bold.

| | Northeast China | | | Inner Mongolia | | | Northwest China | | | North China | | | Central China | | | QTP | | | Southeast China | | | South China | | | Southwest China | | |
|---|---|---|---|---|---|---|---|---|---|---|---|---|---|---|---|---|---|---|---|---|---|---|---|---|---|---|---|
| | n | a | p | n | a | p | n | a | p | n | a | p | n | a | p | n | a | p | n | a | p | n | a | p | n | a | p |
| CABLE | 100 | 2.29 | **0.58** | 100 | 1.54 | 0.06 | 100 | 1.76 | **1** | 100 | 1.63 | 0.02 | 100 | 1.69 | **0.14** | 100 | 1.47 | 0.06 | 100 | 1.66 | **0.59** | 100 | 1.52 | 0.01 | 100 | 1.79 | 0.02 |
| CLM4.5 | 100 | 1.50 | 0.01 | 100 | 3.12 | **0.63** | 100 | 1.61 | 0 | 100 | 1.70 | **0.13** | 100 | 3.36 | **0.51** | 100 | 1.71 | **0.19** | 100 | 1.68 | **0.27** | 100 | 1.78 | 0.09 | 100 | 1.65 | 0.07 |
| DLEM | 100 | 1.82 | **0.16** | 100 | 2.03 | 0.01 | 100 | 2.34 | **0.17** | 100 | 1.69 | 0.02 | 100 | 1.49 | **0.21** | 100 | 1.61 | 0.01 | 100 | 1.57 | 0.03 | 100 | 1.64 | **0.23** | 100 | 1.73 | **0.22** |
| ISAM | 100 | 1.86 | **0.43** | 100 | 1.45 | 0 | 100 | 1.54 | 0 | 100 | 1.78 | **0.10** | 100 | 3.04 | **0.52** | 100 | 5.06 | **0.26** | 100 | 1.61 | 0 | 100 | 1.72 | **0.18** | 100 | 2.35 | **0.20** |
| LPJ-GUESS | 100 | 1.71 | 0.05 | 100 | 1.63 | **0.12** | 100 | 1.82 | 0.01 | 100 | 1.63 | 0.06 | 100 | 1.59 | 0 | 100 | 2.13 | **0.92** | 100 | 1.59 | 0 | 100 | 1.70 | 0.04 | 100 | 1.67 | 0.01 |
| LPJ-wsl | 100 | 1.57 | 0.01 | 100 | 4.83 | **0.61** | 100 | 10.82 | **0.80** | 100 | 1.82 | **0.17** | 100 | 1.57 | 0 | 100 | 2.56 | **0.24** | 100 | 1.70 | 0.01 | 100 | 1.78 | 0.01 | 100 | 1.72 | 0.04 |
| LPX-Bern | 100 | 1.66 | 0.05 | 100 | 1.49 | 0.05 | 100 | 4.66 | **0.80** | 100 | 1.64 | 0.01 | 100 | 1.58 | **0.27** | 100 | 3.05 | **0.82** | 100 | 1.59 | 0.01 | 100 | 1.71 | **0.17** | 100 | 2.19 | **0.44** |
| ORCHIDEE | 100 | 2.27 | **0.20** | 100 | 6.61 | **0.89** | 100 | 2.76 | **0.94** | 100 | 1.61 | **0.12** | 100 | 2.12 | 0.08 | 100 | 2.48 | **0.98** | 100 | 2.19 | 0.08 | 100 | 2.54 | **0.40** | 100 | 1.54 | 0.03 |
| ORCHIDEE-MICT | 100 | 1.59 | 0.05 | 100 | 1.54 | 0.01 | 100 | 1.74 | **0.60** | 100 | 1.49 | 0.01 | 100 | 2.49 | 0.04 | 100 | 1.92 | 0.01 | 100 | 1.92 | 0.03 | 100 | 1.66 | 0.02 | 100 | 2.04 | **0.84** |
| SDGVM | 100 | 1.69 | **0.10** | 100 | 4.77 | **0.93** | 100 | 1.87 | **0.20** | 100 | 1.66 | 0.02 | 100 | 1.87 | 0.09 | 100 | 1.67 | 0.02 | 100 | 1.80 | 0.02 | 100 | 1.79 | **0.64** | 100 | 1.71 | 0.07 |
| VEGAS | 100 | 1.50 | 0.03 | 100 | 1.81 | 0.07 | 100 | 2.34 | **0.83** | 100 | 1.59 | 0 | 100 | 1.65 | 0.01 | 100 | 1.80 | 0.01 | 100 | 1.64 | 0.01 | 100 | 1.76 | 0.09 | 100 | 1.81 | 0.01 |
| VISIT | 100 | 1.55 | 0 | 100 | 1.64 | 0.01 | 100 | 2.54 | **0.93** | 100 | 2.79 | **0.81** | 100 | 1.61 | 0.01 | 100 | 1.83 | **0.25** | 100 | 1.60 | 0.03 | 100 | 1.68 | **0.10** | 100 | 2.35 | **0.28** |
| Yao-GPP | 100 | 1.87 | **0.38** | 100 | 1.54 | 0 | 100 | 1.99 | 0.01 | 100 | 2.13 | **0.10** | 100 | 3.45 | **0.96** | 100 | 3.20 | **0.72** | 100 | 2.22 | **0.18** | 100 | 1.99 | **0.65** | 100 | 2.09 | **0.18** |